

# Geochemistry, Geophysics, Geosystems

## RESEARCH ARTICLE

10.1029/2019GC008815

### Key Points:

- We combine geodynamic modeling with seismic wave propagation to constrain the state of the dynamics underneath the Réunion island
- We analyze the sensitivity of seismic observables to geodynamical parameters
- Our results favor high-melt extraction rates underneath the Réunion island

### Correspondence to:

N. Fuji,  
nobuaki@ipgp.fr

### Citation:

Franken, T., Armitage, J. J., Fuji, N., & Fournier, A. (2020). Seismic Wave-Based Constraints on Geodynamical Processes: An Application to Partial Melting Beneath the Réunion Island. *Geochemistry, Geophysics, Geosystems*, 21, e2019GC008815. <https://doi.org/10.1029/2019GC008815>

Received 13 NOV 2019

Accepted 15 MAR 2020

Accepted article online 4 APR 2020

## Seismic Wave-Based Constraints on Geodynamical Processes: An Application to Partial Melting Beneath the Réunion Island

T. Franken<sup>1</sup>, J. J. Armitage<sup>1,2</sup>, N. Fuji<sup>1</sup>, and A. Fournier<sup>1</sup>

<sup>1</sup>Université de Paris, Institut de physique du globe de Paris, CNRS, Paris, France, <sup>2</sup>Now at: IFP Énergies Nouvelles, 1 & 4 Avenue de Bois Préau, Rueil-Malmaison Cedex, France

**Abstract** The inversion of seismic observations leads to maps of the interior of the Earth that can be interpreted. Regions of low seismic velocity have historically been interpreted to be due to factors related to high-temperature and high-melt retention. Subsequently, geodynamic models can be used to test such interpretations. However, the inversions are nonunique, and arguably, it would be best to test geodynamic scenarios against observations rather than interpretations. Here we make a first attempt at this. At depths greater than 80 km below Réunion, a low shear-wave velocity zone is imaged. Rather than interpret this inverted model, we test a forward model of melt generation and retention against seismic observations. Geodynamic model solutions are converted with a mineral parameter database to *P* wave and *S* wave velocity profiles from various initial temperatures *T*, upwelling velocities  $\bar{v}$ , and permeabilities  $k_0$ . By embedding these velocity profiles, synthetic seismograms are generated. For a range of  $k_0$ , *T*, and  $\bar{v}$ , we generate synthetic traces for 21 teleseismic events registered at a receiver on Réunion island. We measure the traveltimes between observed and synthetic waveforms and the interphase differential traveltimes for 210 scenarios for several phase arrivals of three components, filtered between 0.01 and 0.2 Hz. The results indicate that upper mantle temperatures beneath Réunion lie within 1400–1450 °C, with permeability coefficients of  $10^{-5}$ – $10^{-6}$  m<sup>2</sup>. These conditions are associated with porosities of <0.28% and high-melt extraction rates of 8.37–18.35 m·year<sup>-1</sup>. This study demonstrates the potential for fully comparing geodynamic scenarios with seismic observations.

## 1. Introduction

The geodynamical evolution of planetary interiors at any scale has been constrained by observations made at and/or above the surface of the Earth and planets. Seismological observations, for example, can give some information in the form of a “snapshot” of the structure of Earth’s interior. However, it is seldom the seismological parameters that the geoscience community really wants to know; rather, we use them to attempt to understand thermochemical conditions of the planetary interior and their evolution. This is why most of the studies on the Earth’s interior have been based on inversions of such observations. Here we briefly review the classical inversion procedures. We then present our methodology for forward modeling in geodynamics and seismology. Lastly, we introduce melt migration dynamics beneath Réunion island, to which we applied our methodology.

### 1.1. Inverse Versus Forward Problems in Geoscience

A multidisciplinary approach of exploration of the Earth’s interior using seismology could be expressed as in Figure 1. The classic procedure (light blue arrows in Figure 1) starts from the collection of the seismic raw waveforms  $\mathbf{d}$  (see equation 1). We then filter the observed waveforms and/or extract secondary information such as traveltimes, surface-wave phase velocity, and receiver function. We then invert these filtered data linearly or in a linearized fashion (e.g., seismic tomography and full-wave waveform inversion), in order to obtain an inverted seismological model in terms of density, (an)isotropic seismic velocity, and seismic attenuation. We then interpret the ensemble of seismic parameters as geodynamically meaningful parameters such as temperature and chemical anomalies inside the Earth’s mantle, based primarily on petrological knowledge. The geodynamicists will finally seek the most probable scenario(s) of the Earth’s inner evolution, in order to qualitatively match their “virtual Earth models” to the tomographic “observation”. This workflow (light blue arrows in Figure 1, expressed mathematically as equation A1 within Appendix A) is

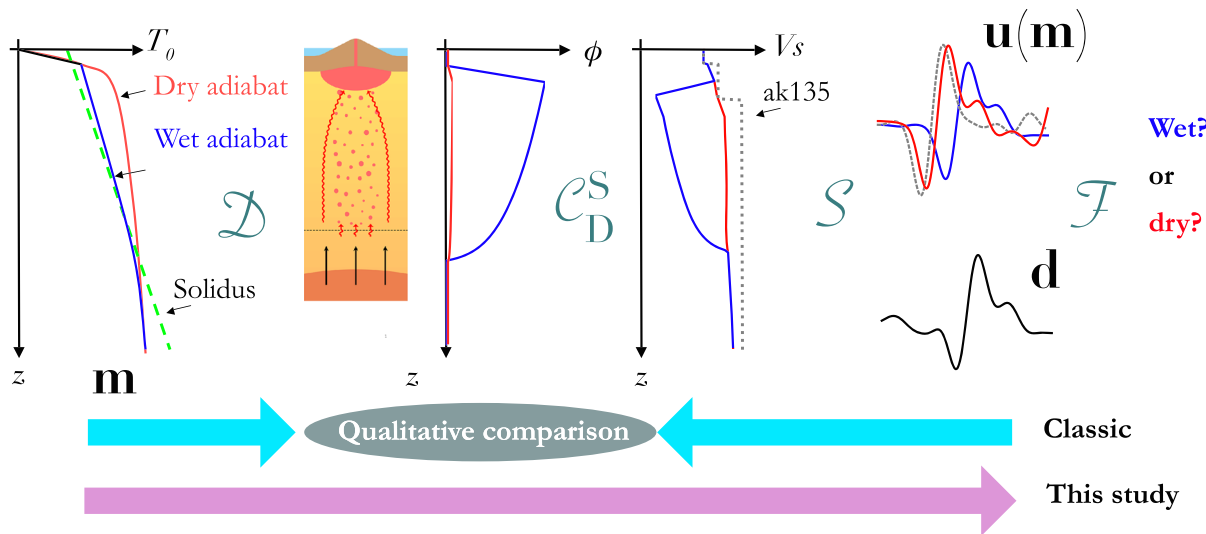


**Figure 1.** Conceptual schema of our waveform seismic filtering strategy (pink arrow for corresponding workflow). On the top from the left to right: we first generate ( $\mathcal{D}$ ) geodynamical scenarios with different initial conditions  $\mathbf{m}$  ( $T_0$ , e.g., wet and dry in blue and red, respectively) in order to obtain a steady-state snapshot (vertical variation of porosity  $\phi$ , for example). We then translate ( $C_D^S$ ) the set of geodynamical parameters such as  $\phi$  to a set of seismological parameters such as  $V_s$ . We then generate ( $\mathcal{S}$ ) seismic waveforms  $\mathbf{u}$  to investigate the sensitivity of  $\mathbf{u}$  with respect to  $\mathbf{m}$ . We define a filter  $\mathcal{F}$  that can distinguish the different scenarios  $\mathbf{m}$ : We then analyze the observed data  $\mathbf{d}$  to select the preferred geodynamical scenario(s). Classical approaches (light blue arrows) try to fit the intermediate parameter sets such as seismic velocity structure or porosity structure that has unknown error bars due to a series of inversion procedures. A detailed discussion can be found in Appendix A.

unavoidable when we do not have sufficient data or a priori information on the Earth's evolution (French & Romanowicz, 2015; Marjanović et al., 2017).

Nevertheless, due to the regularization terms imposed throughout the chain of (localized and) linearized inversions, it is difficult to quantitatively discuss the probability of proposed Earth's evolution scenarios (Atkins et al., 2016; Ritsema et al., 2007). The only way to self-consistently answer this question is to directly model the full problem from first principles and compare the predicted data with the real data, that is, predict a self-consistent thermochemical structure, then predict the seismic properties, and subsequently make a full comparison with the observation. Here the observation is the seismic signal received at the Earth's surface. Following this methodology, we must perform every procedure in a forward manner, and we propose that this approach is more powerful and objective than a series of inversions, in particular when we have geodynamical parameters  $\mathbf{m}$  to investigate (see equation 1).

When we have a concrete set of geodynamical parameters to explore (e.g., degree of contribution of chemical heterogeneity to mantle convection or melt retention beneath a volcanic island, as in this paper), we should be able to directly and quantitatively investigate the appropriateness of each ensemble parameter range,  $\mathbf{m}$ , against the observed seismic waveforms,  $\mathbf{d}$  (equation 1). The crucial element to realize this direct comparison is relying on the capacity of forward modeling. Therefore, we propose to find the direct link between  $\mathbf{m}$  and  $\mathbf{d}$  by a series of forward modeling,

$$\mathbf{u} = \mathcal{S} \circ C_D^S \circ \mathcal{D}(\mathbf{m}), \quad (1)$$

with  $\mathbf{u}$  the “seismically (low-) filtered waveform data” instead of “seismically filtered model” (see the discussion in Appendix A). The operators  $\mathcal{D}$ ,  $C_D^S$ , and  $\mathcal{S}$  denote forward-modeling operators in geodynamics, petrology, and seismology, respectively (see the detailed discussion in Appendix A). Due to the series of forward operators, the sensitivity of  $\mathbf{u}$  with respect to  $\mathbf{m}$  should be reduced: We therefore insist that this operation is “low filtering.” The aim is thus to maximize the sensitivity by choosing a set of attributes from  $\mathbf{u}$ . The operation per se could be costly with respect to a series of inversions, but we can ideally perform a global search instead of local search. As indicated in the red arrow in Figure 1, we will be able to directly compare these “seismically (low-) filtered waveform data,”  $\mathbf{u}(\mathbf{m})$ , as a function of geodynamical model parameters,  $\mathbf{m}$ , and the observed data,  $\mathbf{d}$ .

## 1.2. Melt Migration Dynamics Beneath the Volcanic Regions

For our first attempt to perform “waveform (low-) seismic filtering” (equation 1 and equation A8 in Appendix A), we choose the melt migration dynamics beneath the volcanic regions. Within the Earth’s interior, melting most likely occurs only at the uppermost and lowermost mantle, due to the possible crossings of the mantle rock solidus and the geotherm (Herzberg et al., 2013; Karato, 2014). Within the asthenosphere below mid-ocean ridges, such as the East Pacific Rise (EPR), a seismic low velocity zone (LVZ) is found at depths between approximately 80 and 200 km with several percent of reduction in shear-wave velocity. The origin of such LVZs has been proposed to be due to the presence of partial melt (Stixrude & Lithgow Bertelloni, 2005). Direct comparison with experimental results on rock assemblies of solid olivine and molten basalt infers small amounts of partial melt at 0.1- to 0.3-wt.% levels (Chantel et al., 2016). Also, high-melt transportation velocities ( $20 \text{ m}\cdot\text{year}^{-1}$ ) at mid-ocean ridges are proposed based on U-series isotope study (Elliott & Spiegelman, 2003; Stracke et al., 2006). Yet 2D geodynamical modeling together with a linear estimation on poroelastic effects of partial melt on shear-wave velocity requires a high-melt retention (~0.3–2%) to explain the cause of LVZ obtained from surface-wave tomography at EPR.

The EPR is one of the most studied and well-understood areas of mantle upwelling and magma generation. Seismic observations from the MELT and GLIMPSE experiments at the EPR register a large negative velocity anomaly at the expected depth interval of the primary melting zone (Forsyth, 1998). Based on  $S$  wave travel time delay and Rayleigh wave phase velocity variations, there is an estimated 1–2% of melt present at this interval (Forsyth, 1998). The low seismic velocities modeled below the EPR cannot be replicated with a classic thermal model that only considers conductive cooling (Harmon et al., 2009). This leads to the conclusion that there must be an additional reduction in seismic velocity due to the presence of at least 1% melt, taking the reduction in seismic velocity extrapolated from laboratory experiments (Hammond & Humphreys, 2000).

The question of the quantity of melt retained in the asthenosphere becomes more complicated if attenuation is included (Goes et al., 2012). The base of the LVZ below the EPR is at close to 100-km depth (Harmon et al., 2009). For significant melting to occur at this depth, the solidus needs to be lowered due to increased volatile content (e.g., Hirschmann et al., 1999). The removal of volatiles as they partition into the deep melt will create a region of low  $V_S$  and low  $Q_S$  (high attenuation) that coincides with this deep melting (Goes et al., 2012). Volatile-rich melting is however not productive, and no more than 0.1% melt is typically retained within the asthenosphere at depths between 200 and 90 km (Hirschmann et al., 2009). It is only within the shallow region (<60 km) of silicate melting that larger quantities of melt can be retained (Goes et al., 2012). This shallow region of low  $V_S$  due to melt retention is unresolvable at the resolution of the MELT and GLIMPSE experiments. Therefore, it can be concluded that the LVZ below the EPR is most likely due to the effects of attenuation and not melt retention.

Below volcanic islands such as Hawaii and the Galapagoes, a deep seismic discontinuity has been imaged at depths of 140 to 100 km (Rychert et al., 2013, 2014). This seismic discontinuity is imaged in the form of  $S$ -to- $P$  receiver functions and has been interpreted to represent the onset of deep volatile-rich melting (Rychert et al., 2013, 2014). However, this interpretation is incompatible with forward models of melt generation and transport (Armitage et al., 2015; Havlin & Parmentier, 2014). It was found that the only way to generate a strong seismic discontinuity that could be imaged through  $S$ -to- $P$  receiver functions is if the mantle contains no volatiles (Havlin & Parmentier, 2014). Under such conditions, the rate of melt production is sufficiently high to create a sudden step in porosity that would significantly reduce seismic velocities.

At regions of continental breakup, the same arguments of low  $V_S$  and deep  $S$ -to- $P$  receiver functions have been used to argue for a significant quantity of melt retention (e.g., Rychert et al., 2012). However, just as before, forward geodynamic models have been incapable of matching the tomographic models obtained using seismic inversions. By modeling the composition and volume of melt generated in the Afar region of the East African Ridge, it was found that melt retention in the asthenosphere was most likely no more than 0.5% (Armitage et al., 2015). In general, along the Afar Rift, forward models have found that the magnitude of the observed seismic velocities can be explained without the need for more than 1% melt retention (Armitage et al., 2018, 2015).

Seismic studies consistently infer roughly 1% to 2% melt retention based on, for example, the reduction in  $S$  wave velocity below the EPR (e.g., Harmon et al., 2009), seismic attenuation at the Juan de Fuca and

Gorda ridges (Eilon & Abers, 2017), or to generate the seismic discontinuity observed at the lithosphere–asthenosphere boundary (LAB) in the central Atlantic (Mehouachi & Singh, 2018). There is therefore clearly a disconnect between what forward geodynamic models predict for melt retention (<1%), and the quantity seismic interpretation calls for (>1%). In order to solve this enigma, we propose a series of forward modeling both in geodynamics and in seismology, analyzing one-station teleseismic data at Réunion island to understand the LVZ (of ~4%) based on the partial melt hypothesis. We attempt to predict the observation, the seismic waveform, from the structure predicted by the forward geodynamic model. We will focus on Réunion given that previous studies indicate that this region likely contains some degree of melt within the asthenosphere (Mazzullo et al., 2017). We predict the melt porosity and velocity in a 1D upwelling mantle regime and calculate the corresponding transport velocity of the melt toward the surface. From the 1D model of temperature, pressure, and melt fraction, we predict  $V_p$  and  $V_s$  velocities and use these to generate synthetic waveforms across a range of plausible mantle conditions. Finally, we integrate seismic observations from the Réunion mantle plume for a comparison with the synthetic seismograms to attain a best-fit model in order to constrain mantle permeabilities, melt fractions, and melt flow velocities below Réunion island.

### 1.3. Réunion Island

In this study, we work on the 1D melt dynamics beneath the Réunion island. A recent surface wave seismic tomography model shows evidence for a 4% reduction in  $S$  wave velocity at depths of around 80 km (Mazzullo et al., 2017). This could be indicative of high mantle temperatures and high degrees of melt retention. It is clear that the mantle is melting below La Réunion, but how much is retained within the mantle and contributes to the low velocities found within seismic inversions is unclear.

The first signature of plume activity in the western Indian Ocean dates back to 65–66 Ma in the late Cretaceous during the formation of the Deccan Traps, a large igneous province covering 500,000 km<sup>2</sup> (Courtillot et al., 2003; Duncan & Hargraves, 1990). The ascent of a deep mantle plume and its interaction with the base of the lithosphere, inducing surface volcanism and the formation of the Deccan Traps, are postulated as the beginning of the Réunion hotspot track (Richards et al., 1989). North-eastward plate movement of the African Plate 34 Ma ago created a linear chain of age-progressive islands, forming the Mascarene Plateau, Mauritius, and Réunion. This large oceanic volcanic system is located 800-km east of Madagascar and lies in the southernmost part of the Mascarene Basin. It is therefore assumed that the present-day volcanic activity at the Piton de la Fournaise volcano on Réunion island is the surface expression of the upwelling mantle plume and that there is a large quantity of melt being generated and transported to the surface below this volcanic island.

The petrology and geochemistry of the Piton de la Fournaise lavas can provide information on upper mantle conditions from which they originate, such as the thermal state at formation (Herzberg et al., 2007). As mantle convection drives mantle rock to the surface, fusible components of the peridotitic mantle rock melt at grain boundaries when solidus temperature and pressure conditions are reached. The residual solid matrix becomes a porous medium for fluid flow, where buoyant forces arise from a density differential between the liquid melt and solid matrix and drive melt toward the surface. Although the composition of the melt may be modified during its ascent by fractional crystallization and/or mixing, lava samples can be reconstructed into their primary magma composition from which the MgO content can be used as an indicator of source temperature. Concentrations of MgO are predominantly temperature dependent, meaning magmas with a high MgO content reflect dry and hot source conditions (Hirose & Kushiro, 1993). Geochemical analysis of primary magmas from Réunion formations shows high MgO concentrations of 16–20 wt.%, indicating melting conditions of mantle peridotites at temperatures above 1450 °C (Sobolev & Nikogosian, 1994). Furthermore, a ~2-km-thick underplated magmatic body deduced from receiver function inversions and seismic refraction profiles (Charvis et al., 1999; Fontaine et al., 2015; Gallart et al., 1999) has been proposed to consist of ultramafic primary melt originating from 60- to 90-km depths (Richards et al., 2013).

A high-temperature upper mantle below Réunion is in line with local seismic tomography studies, which confirm a low shear-wave velocity zone (LVZ) below the oceanic crust (Fontaine et al., 2015; Mazzullo et al., 2017). The LVZ phenomenon is not unique to Réunion but has been observed globally below hotspots, rifts, and mid-ocean ridges in areas such as Afar, the East Pacific Rise, Hawaii, the Galapagos, and Iceland. There is abundant evidence for partial melting associated to deep mantle upwelling in these areas. However, the quantity of partial melt and its significance to LVZ remain contested by geodynamic, seismic, and petrologic studies: Are these LVZs purely thermal or require an additional mechanism, such as the presence of partial

melt (e.g., Cobden et al., 2018; Eilon & Abers, 2017; Goes et al., 2012)? The dynamics of the system and the mechanisms responsible for the velocity anomaly remaining poorly understood and other explanations involving upper mantle anisotropy, attenuation, volatile content, solid-state mineralogy, and grain boundary sliding are still being explored.

## 2. Methods

How much melt can be retained in LVZ? Or, more in general, what is the cause of LVZ and its role in whole mantle convection? As we discussed in Section 1, we propose a series of forward modeling through geodynamics, petrology, and seismology, in order to understand the sensitivity of geodynamical parameters to the seismic observations. Seismic inversion studies of the structure beneath the Réunion island have provided valuable results on the quantification of LVZs. Here, our forward modeling approach will allow us to control individual model parameters in geodynamics instead of seismic parameters (see the discussion in Appendix A), in order to test their effects directly on seismic observations: seismic waveforms themselves. We therefore develop a 1D melting model, which is converted to seismic velocities, density, and attenuation, and then, we propagate a seismic wave through models of a range of mantle conditions (equation A8). We explore the sensitivity of geodynamical scenarios to seismic attributes  $\mathcal{F}(\mathbf{u})$  and analyze the observed seismic data to conclude. In particular, in this study, it consists of the four unknowns:

$$\mathbf{m} = (k_0, T_0, \bar{v}, \phi)^T, \quad (2)$$

with  $k_0$  the permeability coefficient,  $T_0$  the initial temperature,  $\bar{v}$  the average upwelling velocity, and  $\phi$  the porosity.

### 2.1. 1D Geodynamical Modeling

The production and transport of melt in the 1D melting system can be described by the following set of modified Stokes equations (McKenzie, 1984; Ribe, 1985). We consider a 1D system where mantle moves upwards and as it does so, it decompresses and melts (Figure 1). The evolution of this system can be described by a set of continuum equations beginning with temperature. The temperature of the system over time is described by a general advection-diffusion equation that incorporates melting as a source term:

$$mL + \rho c \frac{\partial T}{\partial t} + \rho c \bar{v} \frac{\partial T}{\partial z} - \kappa \frac{\partial^2 T}{\partial z^2} = 0, \quad (3)$$

where  $m$  is the melt production rate,  $L$  is the latent heat of melting,  $\rho$  is the density,  $c$  is the specific heat capacity,  $T$  is the temperature,  $\bar{v}$  is the average upwelling velocity,  $z$  is the system depth in kilometers, and  $\kappa$  is the heat conductivity.

The average upwelling velocity consists of a solid upwelling component and a liquid upwelling component, with the mantle rock matrix being the solid and the melt as the liquid component:

$$\bar{v} = (1 - \phi)v_s + \phi v_l, \quad (4)$$

where  $v_s$  and  $v_l$  are, respectively, the velocity of the upwelling matrix and melt and  $\phi$  is the porosity.

Melting of the upwelling mantle rock occurs when its temperature and pressure conditions exceed that of the solidus (Figure 1), which we assume is only a linear function of pressure and is given by

$$T_s = T_{s0} + \frac{\partial T_s}{\partial p} p, \quad (5)$$

where  $T_{s0} = 1080^\circ\text{C}$  and  $\frac{\partial T_s}{\partial p} = 132 \times 10^{-9}^\circ\text{C}\cdot\text{Pa}^{-1}$  (Scott, 1992). We assume that melt production rate  $m$  is governed by the difference in mantle temperature  $T$  and solidus temperature  $T_s$ ,  $\Delta T = T - T_s$ , the latent heat  $L$  from melting, and a depletion term  $\partial T_s / \partial \phi$  that accounts for the increased difficulty to melt-depleted mantle:

$$m = \Delta T \left( L + \frac{\partial T_s}{\partial \phi} \right)^{-1}. \quad (6)$$

The depletion term is generally controlled by mantle composition, where melting becomes more difficult as pyroxenes and clinopyroxenes are extracted from the solid mantle into the melt and the less fusible olivine

remains (e.g., Morgan, 2001). However, since mantle composition is not directly implemented into the 1D model, we approximate depletion using a power law relation:

$$\frac{\partial T_s}{\partial \phi} = C e^{a\phi}, \quad (7)$$

where  $C = 440$  K is a constant for the initial depletion value (Morgan, 2001) and  $a = 5.5$  is a dimensionless depletion coefficient that we use to create a diminishing melt production. Note that  $C$  has a dimension of temperature since porosity is dimensionless. This simplified set of melting relations does not capture the full complexities of multicomponent melting (e.g., Katz et al., 2003; Morgan, 2001). It does however capture the most important aspects of melt generation to allow for a 1D melt transport model and give a simple model solution through which to propagate seismic waves.

The melt transport through the system is approximated as the flow of a liquid phase through a porous medium, which is described by Darcy flow. To create a set of closed equations, we need to approximate for the relationship between permeability and porosity as follows:

$$k_\phi = k_0 \phi^n, \quad (8)$$

where  $k_\phi$  is the permeability and  $k_0$  is the permeability coefficient, with  $k_0$  and  $n$  being constants empirically derived from experiments. At grain-scale melt distributions in partially molten olivine basalts,  $n$  has been empirically determined to be approximately equal to 2.7 for melt fractions of  $\phi > 0.02$  (Miller et al., 2014). The constant  $k_0$  is much more uncertain, with estimates of mantle permeability  $k_\phi$  ranging from  $10^{-15}$  to  $10^{-10}$  m<sup>2</sup> (e.g., Burley & Katz, 2015);  $k_0$  is between  $\sim 10^{-5}$  and  $10^{-10}$  m<sup>2</sup>, assuming  $n = 3$ . Taking the above closure equation in (8), the flow of the melt,  $v_l$ , is subsequently given by

$$\phi(v_l - v_s) = \frac{k_0 \phi^n}{\eta_l} \left( \Delta \rho g + \frac{\partial}{\partial z} p \right), \quad (9)$$

where the term  $\Delta \rho g + \partial p / \partial z$  describes the potential gradient, which drives the flow, where  $\Delta \rho$  is the density difference between fluid and matrix,  $g$  is the acceleration due to gravity, and  $\partial p / \partial z$  is the pressure gradient due to compression of the matrix.

A zero compaction length approximation is adopted, which assumes no contribution of matrix compaction to porous flow. The matrix compression term in equation (9) can be neglected if melt flow is one dimensional and the length scale over which melting occurs is much larger than the reduced compaction length  $\delta_R$  defined as follows (Ribe, 1985):

$$\delta_R = \left[ \frac{\phi_0 \bar{v} \left( \zeta_s + \frac{4\eta_s}{3} \right)}{g \Delta \rho} \right], \quad (10)$$

with  $\zeta_s$  and  $\eta_s$ , respectively, the bulk and shear viscosity of the solid matrix and  $\phi_0$  a reference porosity. Assuming  $\zeta_s$  and  $\eta_s = 10^{15} - 10^{18}$  Pa·s (e.g., Ribe, 1985),  $\Delta \rho = 500$  kg·m<sup>-3</sup> (e.g., Hewitt, 2010), and the reference porosity an estimated range of  $\phi_0 = 0.1 - 5\%$ , we determine an average reduced compaction length for the 1D melting model at 5–50 m, with a maximum upper boundary of 5,000 m for model extremities. The height of the melting column is approximately 80 km, which is three to four magnitudes larger than our estimated reduced compaction length.

We adopt a Boussinesq approximation for the density  $\rho$ , where the density of solid matrix and melt are equivalent except in the buoyancy term (Hewitt, 2010). The conservation of mass for melt is given by

$$\rho \frac{\partial \phi}{\partial t} + \rho \frac{\partial}{\partial z} \phi v_l = m. \quad (11)$$

Under the assumption of a zero compaction length and assuming  $n = 3$ , Darcy's equation (equation 9) can be written as

$$\phi(v_l - v_s) = \frac{k_0 \phi^3}{\eta_l} (\Delta \rho g). \quad (12)$$

To get a solvable equation for melt velocity, we incorporate equation (4) in equation (12) and then substitute this into equation (11) to get a set of equations for melt production and transport as function of porosity:

$$\rho \frac{\partial \phi}{\partial t} + \rho \bar{v} \frac{\partial \phi}{\partial z} + \frac{k_0 \Delta \rho g}{\eta_l} \frac{\partial}{\partial z} [\phi^3 (1 - \phi)] = m. \quad (13)$$

Here  $\bar{v}$  is the imposed upward velocity of the melt and solid matrix, and  $\phi$  is therefore the only unknown, and it therefore can be solved numerically.

## 2.2. Numerical Method for Melt Production and Transport

The 1D partial melting model computes temperature as a function of depth and time through the general advection-diffusion equation (equations 3 and 13), discretized using Crank-Nicolson method. At the depth of 410 km, we initialize the initial mantle temperature ( $T_0$ ) as a fixed temperature boundary condition. At the surface, temperature is fixed at 0 ° C. The model has 410 evenly spaced grid points from 410-km depth to the surface of the Earth. Once the temperature of the system exceeds solidus temperature  $T_s$ , the finite difference scheme determines the production of melt as a function of previous depletion, recalculating temperature according to latent heat from melting for each time step according to equation (6). The third term in equation (13) can be expressed as an advection term  $q \frac{\partial \phi}{\partial z}$  where

$$q = \frac{k_0 \Delta \rho g}{\eta_l} \left[ 3\phi^2 \left( 1 - \frac{4}{3}\phi \right) \right], \quad (14)$$

giving a scheme for calculating  $\phi$  in the next time step as follows:

$$\phi_j^{l+1} = \phi_j^l - \frac{\bar{v}q(\phi_j^l - \phi_{j-1}^l)}{\Delta z}, \quad (15)$$

where superscript  $l$  is the point in time and subscripts  $j$  is the point in space. The free parameters that we will explore are mantle temperature, upwelling velocity, and the permeability coefficient  $k_0$ . Models are run until a steady state is achieved. The melt flow velocity, temperature, and melt production as a function of depth are calculated for a range of scenarios variable upwelling velocities of  $\bar{v}$  (10–70 mm·year<sup>-1</sup>), initial temperatures of  $T_0$  (1250–1500 ° C), and permeability coefficients of  $k_0$  ( $10^{-9}$ – $10^{-5}$  m<sup>2</sup>), at increments of, respectively, 10 mm·year<sup>-1</sup>, 50 ° C, and a factor 10, giving 210 different model scenarios. These parameter ranges describe a series of feasible geodynamic conditions in mantle plume environments.

## 2.3. Conversion to Seismic Properties

At the Earth's surface, we cannot directly “see” the melt retention calculated in the previous section but only the geochemical or seismological observations. In this study we intend to analyze the sensitivity of seismic waveforms with respect to the melt retention. We therefore construct seismological models from geodynamical modeling conducted beforehand. To realize this idea, temperature, pressure, and porosity are converted to isotropic  $P$  wave and  $S$  wave velocities.

To compute seismic velocities for the geodynamical 1D models, we follow the methods of Goes et al. (2012). Phase diagrams and anharmonic velocities are computed using PerpleX (Connolly, 2005) and the equation of state, solid solution models and 2008-NaCFMAS mineral parameter database of Stixrude and Lithgow-Bertelloni (2005) and Xu et al. (2008). Subsequently, we assume that attenuation is given by (Cammarano et al., 2003; Goes et al., 2012)

$$Q = A\omega^\alpha \exp\left(\frac{\alpha\gamma T_s}{T}\right). \quad (16)$$

This Arrhenius style attenuation relationship is empirical, where the melting temperature  $T_s$  is used as an alternative to estimating the depth dependence on activation volume (Karato, 1993). The constants are  $A = 0.1$ ,  $a = 0.15$ , and  $\gamma = 38$ , and we set  $\omega = 2\pi/20.0$  (with a dominant period of 20 s). Since we use large band-pass filters from 100 to 5 s and apply a frequency-independent attenuation during our synthetic seismogram computation, we used this ad hoc value in order that the attenuation remains in the range of ±20% of Arrhenius attenuation described above for all the frequencies. The anharmonic velocity and anelastic contributions are subsequently combined to give the seismic velocity (Goes et al., 2012):

$$V = V_{\text{anh}} \left[ 1 - \frac{Q^{-1}}{2 \tan(\pi\alpha/2)} \right]. \quad (17)$$

Finally, to include the effect of melt, we follow a convention of a 3.6% and 7.9% velocity reduction per percent melt for, respectively, the *P* wave and *S* wave velocities according to Hammond and Humphreys (2000), where the velocity derivatives are based on an organized cuspate pore geometry with relaxed elastic moduli to model a maximum possible effect of melt on seismic wave velocity. Teleseismic waves excite the relaxed modulus of partially molten upper mantle rock, and therefore, we assume relaxed, pressure-equilibrated melt conditions when relating seismic velocity reduction to the mantle physical state (Hammond & Humphreys, 2000).

Wave velocities at depths below 410 km are set to *ak135* (Kennett et al., 1995), since the mineral database only covers the upper mantle up to the Moho. We assume no percolation of melt into the crust and set the model porosity to 0% at the Moho to crudely simulate extraction for simplicity purposes. This is somewhat artificial as there will be a degree of melt storage within the crust in the form of sills and melt lenses. However, it is beyond the scope of the 1D model developed here to examine these processes. Given the wavelength of seismic waves used to probe the structure of the lithosphere and asthenosphere to understand melt retention, we believe that this region can be assumed to be similar to *ak135*. An artifact from this approximation might be a sharp porosity discontinuity at the top of the LVZ, which is modified into a more gradual porosity transition as seen from observations to avoid overestimation of the impedance contrast during synthetic waveform generation. Perceived from seismic tomography results from the Réunion mantle plume, the LVZ starts at about 27-km depth and reaches a minimum velocity at 32-km depth (Fontaine et al., 2015). We apply a moving average filter over this depth range to smooth the top of the porosity curve. The bottom of the model space is truncated at 410-km depth to coincide with the 410-km discontinuity in *ak135* reference model.

#### 2.4. Seismological Modeling

In order to compute full-wave synthetic seismograms for a number of given 1D Earth models in this study up to as high frequency as 1 Hz, we use direct solution method (DSM) (Geller & Ohminato, 1994; Geller & Takeuchi, 1995; Kawai et al., 2006). The DSM obtains the solution of the weak form of the equation of motion by directly solving the Galerkin weak form of the equation of motion:

$$(\omega^2 \mathbf{T} - \mathbf{H})\mathbf{c} = -\mathbf{g}, \quad (18)$$

with  $\omega$  the angular frequency and  $\mathbf{T}$  and  $\mathbf{H}$  the mass and stiffness matrices, respectively.  $\mathbf{g}$  is the external force vector, and  $\mathbf{c}$  is the expansion coefficient of the displacement. We choose the spherical harmonics along the lateral directions of the Earth and linear spline along the vertical direction for basis and trial function expansion of all the vectors and matrices described above. This finite element formulation adheres to natural boundary condition (free surface boundary) and fluid-solid boundary conditions. Numerical dispersion due to the discretization can successfully be eliminated through implementation of optimally accurate operators (Geller & Takeuchi, 1995). The ellipticity of the Earth is also taken into account. The reader can refer to the literature cited herein for further theory, and the extension of DSM to 3D Earth models can be found in Cummins et al. (1997), Fuji et al. (2012), and Monteiller et al. (2015).

The reference Earth model we use for DSM consists of 1D *ak135* model (Kennett et al., 1995). By embedding velocity profiles from our converted models into the reference model at the 12- to 410-km depth range, we generate different sets of synthetics for several source events while varying upper mantle temperatures, upwelling velocities, and permeabilities. The time window is set to a length of 3,276.8 s to include surface waves at high-offset source events, in order to avoid numerical artifacts from superimposition of surface wave energy out of the time window. We calculate seismograms up to 0.3125 Hz so that we can filter them up to 0.2 Hz to compare against the observed waveforms. It is worth noting here that DSM naturally prefers a time window of 0.1 s times a power of 2 in order for the inverse Fourier transform to be free from numerical errors. In this study we consider only isotropic homogeneous media since we will analyze teleseismic phases upgoing through the melt conduit beneath Réunion island.

#### 3. Seismological Data

We would like to extract the geodynamical information from the direct observation on the Earth's surface. Unlike current seismic tomography that makes use of a tremendous amount of data, we would like to extract as much information as possible from a small number of data (21 earthquakes with only one seismic station

**Table 1**  
*Receiver Information RER GEOSCOPE Seismic Station*

Receiver	Latitude (degrees)	Longitude (degrees)	Elevation (m)	Channels	Sampling rate (Hz)
GEOSCOPE RER	-21.17	155.74	834	BHZ, BHN, BHE	20

in Réunion island) to detect signatures from differences in geodynamical scenarios within each individual seismological datum. In this study we will initially focus on the sensitivities of different combinations of permeability, temperature, and upwelling velocity on the synthetic waveform. Furthermore, we compare the synthetic seismograms for each source event with seismic observations acquired from Réunion. The synthetics are generated using DSM according to source and receiver configurations of the seismic observations of the Réunion mantle plume in order to place the models in the context of the Earth.

### 3.1. Receiver

Earthquake observation data are obtained from the GEOSCOPE Observatory, a global network of broadband seismic stations transmitting real-time seismic data to the Institut de Physique du Globe de Paris (IPGP) data center, from which the data are managed and distributed (Douet et al., 2016). It comprises a network of 34 seismological stations in 18 different countries and offers a catalog of earthquakes registered between 2006 and 2018 with magnitudes above 5.5–6. All stations are equipped with three broadband seismometers type STS1 or a three-component seismometer-type STS2, a digitizer, and a local storage system for the data (Douet et al., 2016).

Seismic data are acquired from the GEOSCOPE RER seismic station (Table 1), which is part of the GEOSCOPE Observatory network. This seismic station is situated directly above the upwelling plume on top of the Piton de la Fournaise volcano, capturing seismic waves that have traveled through the LVZ that should contain information on the melting zone. Table 1 contains the receiver specifications for the RER receiver. The seismic observations of interest are recorded as time series data on the broadband seismometer channels of the RER station.

### 3.2. Seismic Sources

From the entire earthquake catalog registered at the RER GEOSCOPE station between January 2006 and December 2015, a selection of events is used for synthetic waveform generation (Figure 2). The selection criteria to decide on adequate source events are based on their source depth, epicentral distance from RER station, signal-to-noise ratio, and clarity of the phase arrivals. To avoid seismic interaction with potential upper-mantle and crustal interfaces and/or melting at the source location, we select deep earthquakes with a source depth greater than 300 km so that the upper mantle effects for observed and synthetic seismograms are only on the RER station side (see Figure 2). We ensure teleseismic incidence at the receiver location by selecting source events at epicentral distances at least beyond 30° (Bormann, 2012). The epicentral distance range of the seismic sources used in this study is from 60° to 120°. In order for an automated waveform correlation to function, we require relatively high signal-to-noise ratio and high amplitude *P* and *S* phase arrivals up to a level where the signal is not masked by noise. Source half-duration time should not exceed the period at which it has been band-pass filtered since the synthetics are simulated with a heavyside source time function, which we will convolve with the source time function provided by SCARDEC (see section 4.2). Table 2 displays the seismic events from the RER GEOSCOPE catalog, which satisfy all the criteria.

### 3.3. Data Processing

Seismic observations acquired from the RER station are deconvolved with the instrument response of the receiver before being subjected to further processing. Hereafter, the north and east horizontal components seismograms are rotated, respectively, along and perpendicular to the great circle path into their radial and transverse components in order to separate the *P-SV* waves from *SH* waves.

Both the synthetics and seismic observations are subjected to a band-pass filter, exploring upper corner frequencies of 0.05 to 0.2 Hz (i.e., lowest periods of 20 to 5 s) with a lower bound kept constant at 0.01 Hz (i.e., 100 s). At frequencies beyond 0.2 Hz, the automated cross-correlation algorithm that compares wave arrivals becomes unstable due to increasing discrepancies related to short-wavelength structure. This automated comparison between synthetic and observed data is set up through automated phase

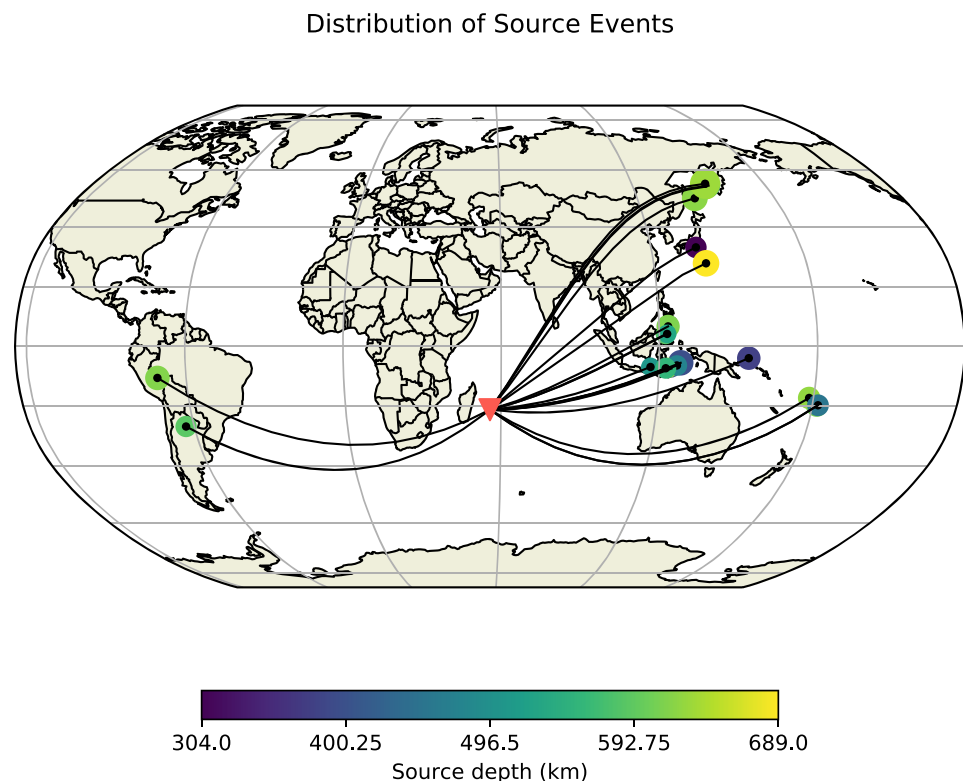


**Figure 2.** Geographical distribution of source events (Table 2). Depth is displayed by color, and earthquake magnitude by size of the circular markers. The location of the RER GEOSCOPE receiver is marked by a red inverted triangle.

picking and time window selection. The cross-correlation time window is chosen based on three factors: (a) the maximum band-pass frequency, where the smallest wavelength is determined through Nyquist theorem; (b) windowing range is set to be a quarter of the dominant period; and (c) a trailing window to account for variation throughout all source events. The precursor is essential to capture a length of flat signal foregoing the phase arrival, which significantly improves distinction between the phase arrival and any arbitrary sinusoidal signal. The trailing windows have been empirically set to 10 s for *P* waves and 20 s for *S* waves and are predominantly required to account for variation in wavelengths between source events and waveform widening caused by high-melt models.

Phase picking is initiated through TauP method (Buland & Chapman, 1983; Crotwell et al., 1999), in order to compute theoretical travel time arrivals for each seismic phase for a given earth model. TauP enables us to center the cross-correlation time window on a given phase of the *ak135* synthetic trace. We proceed to find the time shift between this phase in *ak135* and the presumed phase arrival in the data traces and all synthetic model traces by cross correlating the two traces. The time shift is used to shift the cross-correlation window to the phase arrivals for each seismic and synthetic trace, allowing for comparison of phase arrivals between data and models in order to find seismic travel time delay  $t_{P,S}^{\text{shift}}$ . We compute the differential travel time between the *P* and *S* arrival for both the observed seismic trace and synthetic trace and define the residual between the two as  $t_{S-P}^{\text{obs,syn}}$ . Since melt affects seismic velocity reduction for *P* and *S* waves differently, matching the interphase differential travel time of the observed waveforms with the models can help to put a constraint on porosity. Although phase arrivals vary in time with source depth and epicentral distance, we find that relative time travel differences between synthetic and observed traces, such as  $t_{P,S}^{\text{shift}}$  and  $t_{S-P}^{\text{obs,syn}}$ , are insensitive to varying source depth between 300 and 700 km and are virtually unaffected by changes in epicentral distance at the offsets used in this study ( $\sim$ 0.001- to 0.01-s decrease per degree).

**Table 2**

List of 21 Events Used in Our Analyses

#	Source event	Date (yyyy/mm/dd)	Time (hr:min:s)	Latitude (degrees)	Longitude (degrees)	Epicentral distribution (degrees)	Depth (km)	Magnitude	HD (s)
1	Bali Sea	2011/03/10	17:08:36	-6.87	116.72	60.51	510	6.6	4.8
2	Fiji Islands	2006/01/02	22:13:40	-19.93	-178.18	113.15	609	7.1	9.3
3	Banda Sea	2006/01/27	16:58:53	-5.47	128.13	71.62	397	7.7	16.0
4	Sea of Okhotsk	2008/07/05	02:12:04	53.88	152.89	111.11	636	7.7	17.3
5	Sea of Okhotsk	2008/11/24	09:02:58	54.2	154.32	111.98	518	7.3	10.9
6	Banda Sea	2008/12/06	10:55:26	-7.39	124.75	67.81	404	6.5	3.9
7	Honshu	2009/08/09	10:55:55	33.17	137.94	95.26	304	7.0	8.3
8	Banda Sea	2009/08/28	01:51:20	-7.15	123.43	66.66	633	6.9	6.8
9	Celebes Sea	2009/10/07	21:41:13	4.08	122.37	69.92	587	6.8	5.9
10	Fiji Islands	2009/11/09	10:44:55	-17.24	178.33	111.88	626	7.2	10.5
11	Mindanao	2010/07/23	22:08:11	6.72	123.41	71.96	615	7.3	11.0
12	Santiago Del Estero	2011/01/01	09:56:58	-26.8	-63.14	103.84	590	7.0	8.0
13	Celebes Sea	2011/02/10	14:39:27	4.2	122.97	70.52	533	6.6	4.5
14	Banda Sea	2011/08/30	06:57:41	-6.36	126.75	70.03	476	6.9	6.7
15	Sea of Okhotsk	2012/08/14	02:59:38	49.8	145.06	105.59	622	7.7	17.8
16	Sea of Okhotsk	2013/05/24	05:44:49	54.9	153.28	111.46	632	8.3	35.7
17	New Ireland	2013/07/07	18:35:30	-3.92	153.92	96.18	379	7.4	10.9
18	Fiji Islands	2014/11/01	18:57:22	-19.69	-177.76	113.61	455	7.1	8.7
19	Flores Sea	2015/02/27	13:45:5	-7.297	122.54	65.77	557	7.0	7.5
20	Bonin Islands	2015/05/30	11:23:02	27.84	140.49	95.35	689	7.8	20.7
21	Peru-Brazil Region	2015/11/24	22:45:38	-10.54	-70.94	118.79	617	7.5	16.6

Note. Half-duration (HD) times have been taken from Global CMT.

## 4. Results

### 4.1. 1D Melting Model

The melting model calculates porosity and the depth profile of temperature for all combinations of the free parameters explored in Figure 3, resulting in 210 geodynamic model scenarios. For each model scenario, the model temperature, pressure, and porosity as a function of depth are converted to seismic wave velocity according to section 2.3. Seismic wave velocities reduce gradually with reducing depth due to a general decrease in density and the increasing attenuation of the seismic wave due to temperature effects (Goes et al., 2012). At pressure-temperature conditions above the solidus, the presence of melt reduces seismic wave velocity in line with the empirical velocity reduction taken from Hammond and Humphreys (2000). As a result, the models with lower permeability coefficients that create greater melt retention have a larger reduction in seismic wave velocity (Figure 4). We take an example case of a basal temperature of 1450 °C and upwelling rate of 70 mm·year<sup>-1</sup> to describe the modeled vertical porosity and the generated seismic velocity profiles (Figure 4). The depth of the initiation of melting is predominantly controlled by temperature and lies at roughly 85 km if the basal temperature is fixed at 1450 °C. Lower temperatures will yield a shallower onset of melting. Depending on the assumed permeability, the onset of melting can be marked by a sharp increase in porosity. In particular, if the permeability is low, say, when  $k_0 = 10^{-9}$  m<sup>2</sup>, a porosity greater than 2% can be rapidly achieved under these conditions (Figure 4). This is equivalent to a permeability of  $8 \times 10^{-15}$  m<sup>2</sup> in equation (8). At the other end of spectrum, if we assume a high permeability  $k_0 = 10^{-5}$  m<sup>2</sup>, porosity is between 0.1% and 0.5%, which means that permeability is between  $10^{-14}$  and  $10^{-12}$  m<sup>2</sup>. This range of permeability is within the range or higher than those experimentally observed in high-temperature high-pressure experiments (e.g.,  $10^{-16}$  m<sup>2</sup> for a porosity of 2%, Miller et al., 2014, or  $10^{-14}$  m<sup>2</sup> for a porosity of 5%, Connolly et al., 2009).

If we compare the mean porosity from the range of input parameters, we find that in general, the assumed permeability coefficient has the most dominant role in controlling retained melt volumes, over initial

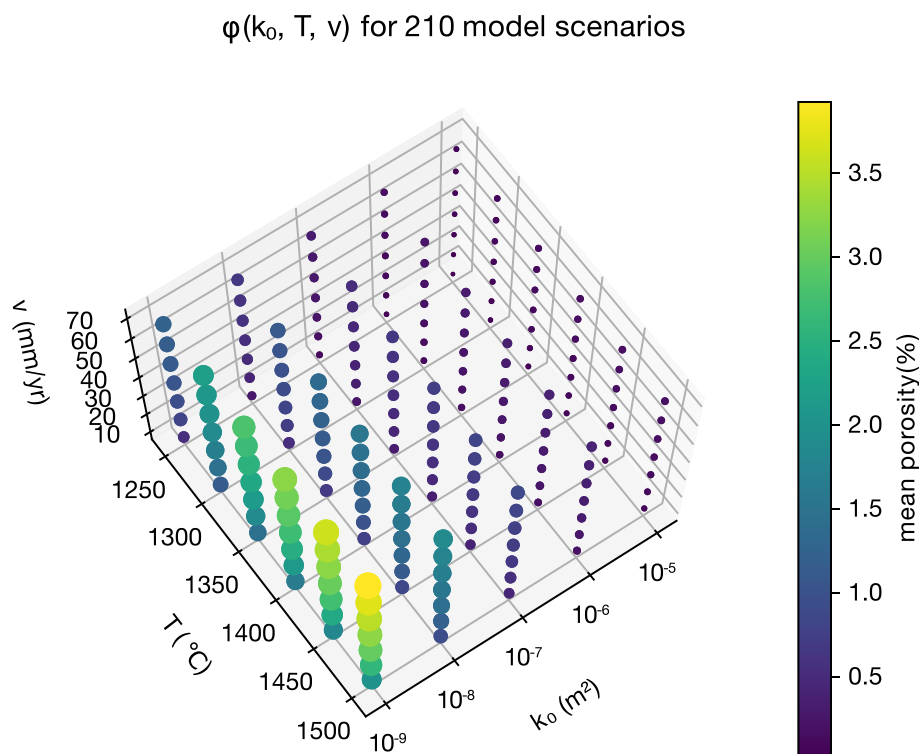


**Figure 3.** The geodynamic model scenarios considered in this study are represented by scatterpoints for each combination of the free parameters  $k_0 = 10^{-9} - 10^{-5} \text{ m}^2$ ,  $T_0 = 1250 - 1500^\circ\text{C}$ , and  $\bar{v} = 10 - 70 \text{ mm}\cdot\text{year}^{-1}$ , giving a total of 210 model scenarios. The mean porosity for each model scenario is illustrated by both scatter color and size.

temperature and upwelling velocity (Figure 5). The latter two parameters appear to have an approximately linear effect on melt porosity, with temperature being the more controlling parameter of the two, according to the contour gradients between Figures 5a and 5b and the dominating horizontal trend in Figure 5c. We observe a slight increased melt production gradient with temperature from slight narrowing in vertical contour spacing in Figure 5a. However, change in porosity is largely driven by permeability coefficient. The smaller the permeability coefficient, the larger the porosity, which can be found in narrowing of the contours in Figures 5a and 5b.

Over the tested permeability range, the mean porosity ranges from 3.92% at the minimum permeability case to 0.03% at the maximum permeability case (Figure 6). The minimum and maximum mean melt transport velocity values over our input range are, respectively,  $0.011 \text{ m}\cdot\text{year}^{-1}$  at minimum permeability and temperature and  $36.77 \text{ m}\cdot\text{year}^{-1}$  at maximum permeability and temperature, with a local velocity maximum peaking at  $90.98 \text{ m}\cdot\text{year}^{-1}$  for the maximum. Melt flow velocity is inversely proportional to melt porosity as a function of  $k_0$  (Figure 7 Weatherley & Katz, 2016). This is because the increased connectivity enhances the flow of melt, allowing for higher melt flow velocities. Melt is extracted and transported to the surface more rapidly, resulting in a lower retention of melt at the onset of melting. Hence, more efficient removal of melt avoids melt accumulation, decreasing maximum porosity with the increase of permeability. U-series disequilibrium studies constrain melt flow velocities at  $\sim 20 - 50 \text{ m}\cdot\text{year}^{-1}$  from short lived  $^{266}\text{Ra}$  excesses (Elliott & Spiegelman, 2003; Stracke et al., 2006). Melt velocities of such magnitude point toward high permeability coefficients ( $k_0 = 10^{-6} - 10^{-5} \text{ m}^2$ ), which would mean low melt porosity below 0.3% and permeability of  $10^{-14} \text{ m}^2$ .

#### 4.2. Synthetic Seismograms

For all 21 source events listed in Table 2, we generate synthetic seismograms. The source adopts the moment tensor of the respective event and is propagated through the range of 1D models for the different mantle temperatures, upwelling velocities, and permeability coefficients, resulting in 210 sets of seismograms per source event (recall Figure 5). The synthetics are convolved with the source time function of their respective source event, since DSM uses a delta function as its moment rate function. Source time functions for

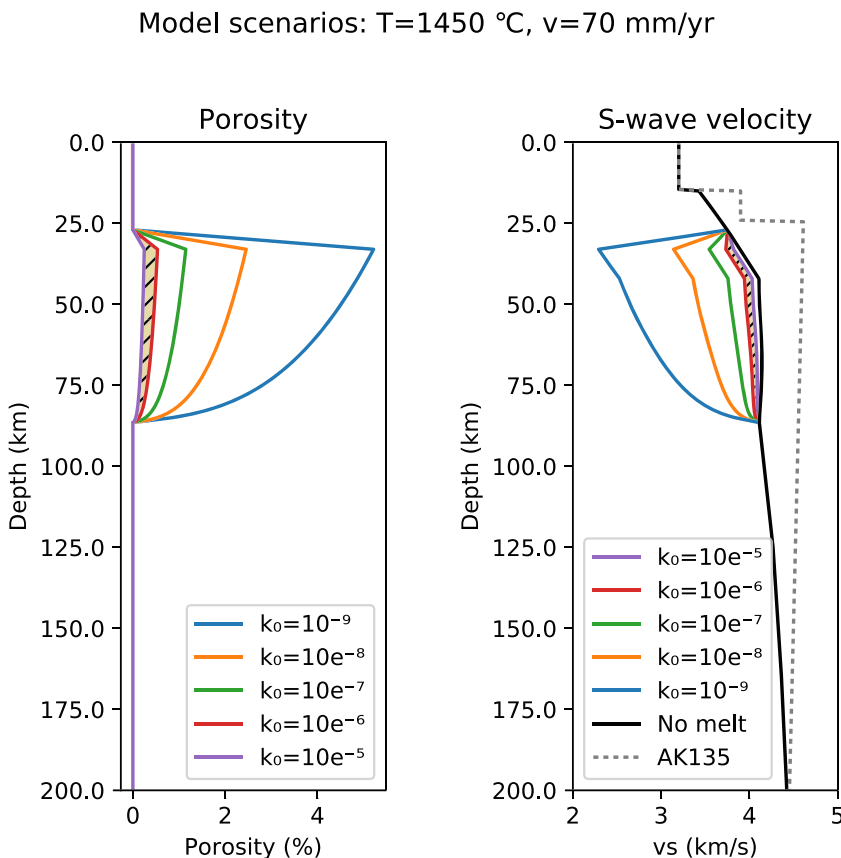


**Figure 4.** Porosity and S wave velocity as a function of depth for the range of permeability coefficients explored in Figure 3, with temperature and the upwelling rate fixed at, respectively, 1450 °C and 70 mm-year<sup>-1</sup>. The velocity profile for the ak135 reference model is shown in gray, and velocity profile for a model without melt is shown in black. The hashed area between the porosity and velocity profiles indicates the most probable model obtained during our “waveform filtering” inversions for the partial melting beneath Réunion island according to this study. At 30-km depth, melt is assumed to leave the system, as here it is probable that the porous flow is no longer a valid assumption for the transport of melt.

each source event were acquired through the SCARDEC source time functions database (Vallée & Douet, 2016). Convolution with the source time function will adjust phase arrivals in time. For source events with a half-duration time higher than the band-pass filtering frequency period, convolution with the source time function will be especially important for accurate prediction of the observed waveforms.

In the upcoming synthetic waveform analysis, we focus on the *P* wave and *S* wave arrivals or the Pdiff and SKS phase arrivals, depending on the epicentral distance of the respective event. The epicentral distances between sources and receiver range from 60° to 120°. At epicentral distances beyond 100°, *P* waves are no longer direct but begin to diffract along the core-mantle boundary and are registered as a Pdiff phase. Similarly, *S* waves are also no longer direct beyond a 100° epicentral distance as well. However, we find that in the epicentral distance range of 100°–120°, the SKS phase experiences less interference with other phases and has higher amplitude arrivals than the Sdiff phase for source events at 300- to 700-km depth.

During synthetic waveform analysis, we investigate four different frequency bands. Waveforms are band-pass filtered from 0.01 Hz to upper limits of 0.05, 0.1, 0.15, and 0.2 Hz.

For each considered event, phase arrival, and wave component, the 210 synthetic models (Figure 7) are cross-correlated with the seismic observation to find the time shift between the two traces. Travel time delay  $t_{P,S}^{\text{shift}}$  of the model with the observation is plotted against the interphase differential travel time  $t_{S-P}^{\text{obs,syn}}$  in order to constrain model scenarios in time (Figure 8). In most cases, the travel time delay and differential travel time do not line up at 0 simultaneously, giving a range of likely model scenarios in between  $|t_{S-P}^{\text{obs,syn}}|$  at  $t_{P,S}^{\text{shift}} = 0$  and  $|t_{P,S}^{\text{shift}}|$  at  $t_{S-P}^{\text{obs,syn}} = 0$ . We define the best-fit models for a given phase arrival by simultaneously

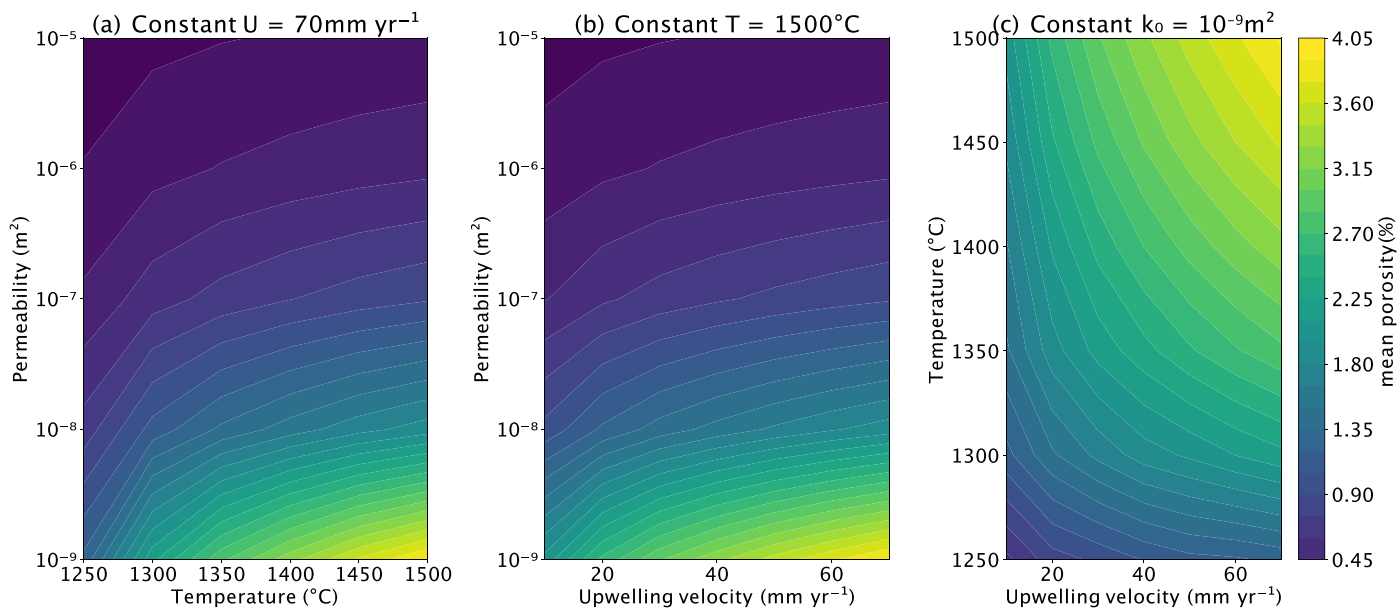


**Figure 5.** Development of porosity over full range of input parameters  $k_0$ ,  $T$ , and  $\bar{v}$ . (a) Temperature versus permeability coefficient at a constant upwelling velocity of  $70 \text{ mm year}^{-1}$ . (b) Upwelling velocity versus permeability coefficient at a constant temperature of  $1500^\circ \text{ C}$ . (c) Upwelling velocity versus temperature at a constant permeability coefficient of  $10^{-9} \text{ m}^2$ .

minimizing  $|t_{P,S}^{\text{shift}}|$  and  $|t_{S-P}^{\text{obs,syn}}|$  through minimizing the combined quadratic mean (RMS) of the two variables (Figure 8). The RMS will be minimal for instances where  $|t_{P,S}^{\text{shift}}|$  and  $|t_{S-P}^{\text{obs,syn}}|$  are equal, which is preferable since the two variables are inherently coupled, where the inability to match one of them is related to the other.

Additional quality checking was conducted during the picking of best-fit model scenarios among all sets of events, phases, components, and band-pass filter bandwidths. Sets are removed if the models deviate from the expected pattern displayed (red points in Figure 8), which means that cross correlation between observation and models has failed to identify the correct arrival. Automated cross correlation of seismic phases is a sensitive process that is prone to failure if the circumstances are not close to ideal. If the observed signal does not possess a high signal-to-noise ratio, clear and high amplitude phase arrivals, a distinct source time function, and all together a high similarity with the synthetic trace, cross correlation is not guaranteed to work accurately. Cross correlations at band-pass filter bandwidths of 0.01–0.05 Hz performed poorly and were omitted in their entirety, whereas cross correlations for the other frequency bands tend to improve with increasing frequency. From the initial 21 source events, only 12 events passed the quality check. A majority of the excluded sources are high offset events with epicentral distances greater than  $110^\circ$ .

#### 4.3. Comparison Against Seismological Observations

In order to discover which modeled melting scenario describes the upper mantle below Réunion most adequately, we will analyze the distribution of best-fit scenarios among the free model parameters  $k_0$ ,  $T$ , and  $\bar{v}$  for the remaining source events that passed quality checking. The best-fit conditions are, however, nonunique solutions, since the porosity we aim to constrain is a function of all three input parameters. Certain trade-offs between  $k_0$ ,  $T$ , and  $\bar{v}$  will have the same outcome in porosity.

By cross-correlating synthetic traces for 210 model scenarios with the seismic observation for 12 source events, compiled for four phase arrivals (P, S, Pdiff, and SKS), three wave components (Rs, Ts, and Zs), and all the band-pass filter frequencies (upper corner frequencies of 0.05, 0.1, 0.15, and 0.2 Hz), we conducted a total 70,896 synthetic to observed phase comparisons, of which we consider 40,950 cases where cross correlation between phases was successful. From these 40,950 cases, there were 1,116 best matches in time between observed and synthetic waveforms, which form a distribution around the most probable model scenario to describe the upper mantle beneath Réunion among the 210 model scenarios. The changes in porosity caused by alterations in upwelling velocity are too insignificant to constrain a specific value of  $\bar{v}$ , and all values of

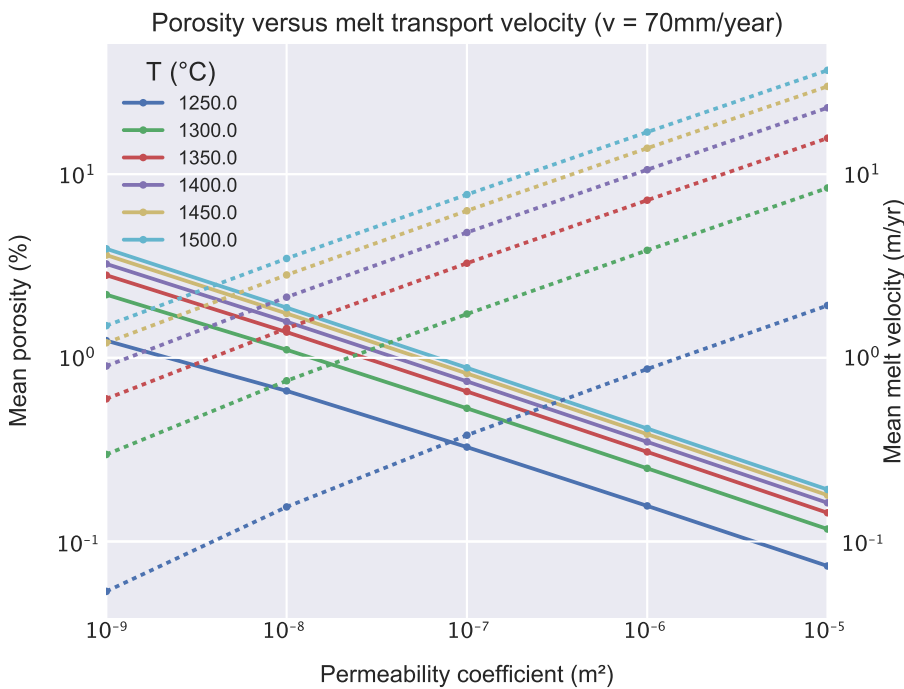


**Figure 6.** Logarithmic plot of the variation in modeled porosity (solid) and melt flow velocity (dashed) with permeability coefficient and temperature, with upwelling velocity constant at 70 mm·year<sup>-1</sup>. The relationship between porosity and mean melt flow velocity is inversely proportional as a function of the permeability coefficient and proportional as a function of temperature.

$\bar{v}$  are equally represented for the entire range of temperatures and permeability coefficients (Figure 9). The results indicate that most best-fit scenarios are covered by the temperature range of 1350–1450 °C. There is a gradual preference to higher permeabilities, although all permeability coefficients are covered. That is because the time delay is a product of melt, which is largely controlled by the permeability coefficient, and the intrinsic anelasticity that increases with temperature. For each permeability, there is a temperature counterpart, which will result in a similar travel time delay. High temperatures are coupled with high permeability coefficients, where the travel time delay is dominated by temperature attenuation. On the other hand, there are the melt dominated cases where low temperatures are coupled with low permeabilities. The  $T \cdot k_0$  relationship in Figure 9 suggests that permeability coefficients of  $k_0 = 10^{-9} \text{ m}^2$  are generally coupled with  $T = 1300 \text{ }^\circ\text{C}$ ,  $k_0 = 10^{-8} \text{ m}^2$  with  $T = 1350 \text{ }^\circ\text{C}$ ,  $k_0 = 10^{-7} \text{ m}^2$  with  $T = 1350 – 1400 \text{ }^\circ\text{C}$ ,  $k_0 = 10^{-6} \text{ m}^2$  with  $T = 1400 – 1450 \text{ }^\circ\text{C}$ , and  $k_0 = 10^{-5} \text{ m}^2$  also with  $T = 1400 – 1450 \text{ }^\circ\text{C}$ . At higher permeabilities, the temperature regimes become indistinguishable because the melt percentages are so low that the travel time delay is dominated by the effect of temperature. These five clusters make up the possible conditions in the upper mantle below Réunion that can explain our chosen set of seismic observations. The mean melt porosity for each cluster is with increasing permeability coefficient, respectively, 1.88%, 1.11%, 0.58%, 0.29%, and 0.13%. Depending on the upper mantle temperature, each of these melt scenarios is a viable solution. The data suggest that most likely, temperature is 1400–1450 °C, based on the combined number of matches with  $k_0 = 10^{-5} – 10^{-6} \text{ m}^2$  with respect to the number of other matches. Second, the mean travel time delay and mean differential travel time for each cluster are minimal for  $k_0 = 10^{-6} – 10^{-5} \text{ m}^2$  at  $t_{P,S}^{\text{shift}} = 0.06 \pm 0.51 \text{ s}$  and  $t_{S-P}^{\text{obs,syn}} = -0.20 \pm 0.46 \text{ s}$ , supporting a mantle temperature of  $T = 1400 – 1450 \text{ }^\circ\text{C}$ . Under these conditions, we can expect porosity of maximum 0.28.

## 5. Discussion

In this study, we proposed a series of forward modeling from geodynamical modeling to seismic waveform computation (equation A8). Instead of collecting a big data set, we first settled the geodynamical parameters to explore (equation 2). The consequences are that we were able to generate seismological models  $C_D^S \circ D\mathbf{m}$  that are geodynamically consistent. Hereafter, we discuss our results in detail.

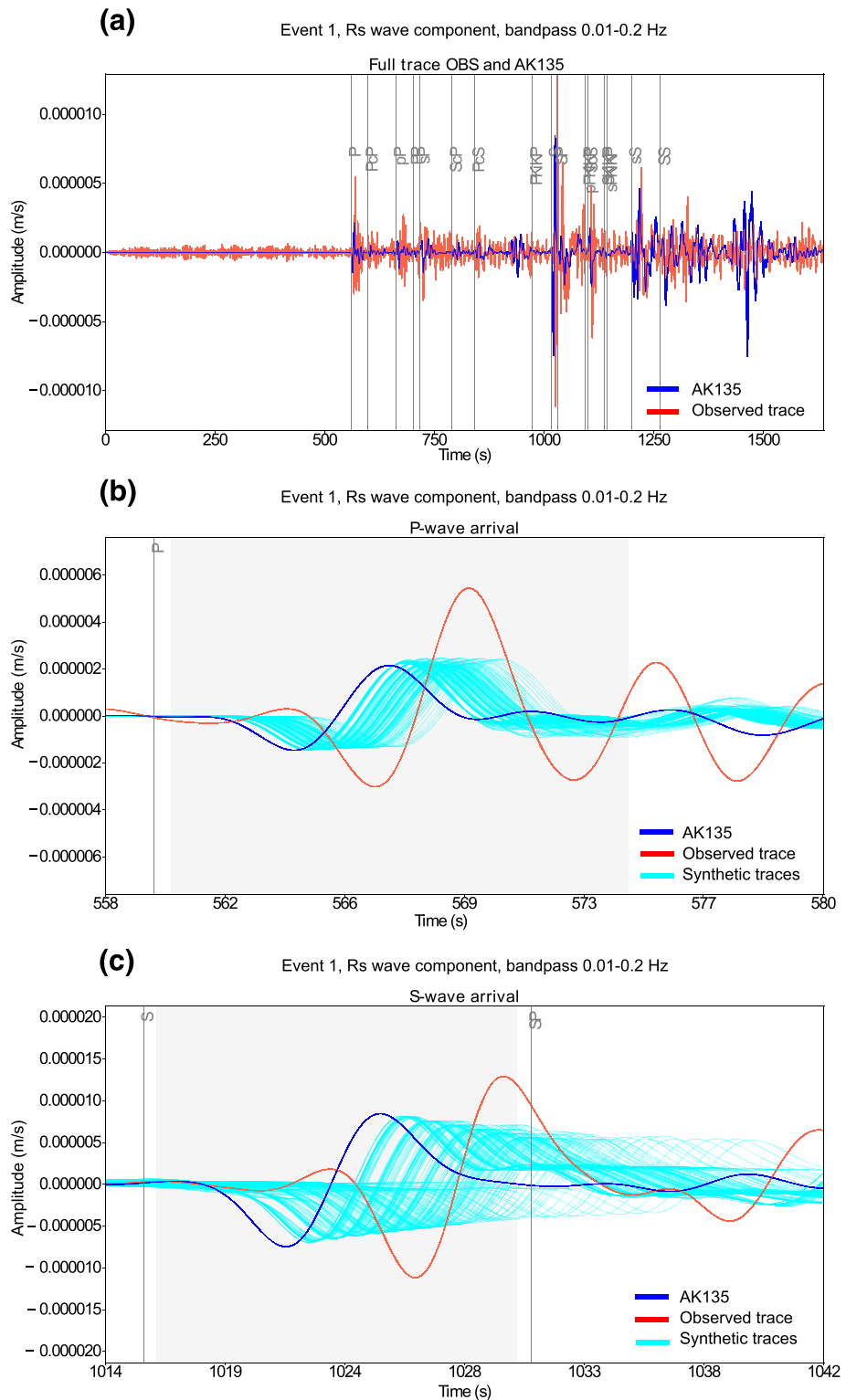


**Figure 7.** (a) Seismogram containing the radial components of the full synthetic waveform generated for *ak135* base model (blue) and the observed seismic trace (red) for event 1, band-pass filtered from 0.01 to 0.2 Hz. (b) A close-up of the *P* wave arrival of trace presented in (a), with the additional 210 synthetic traces (light blue) generated for our melting models. The gray zone represents the automated cross-correlation window used to find the time shift with the observed trace. (c) The equivalent of (b) for the *S* wave arrival.

Relative travel times between observed and synthetic traces

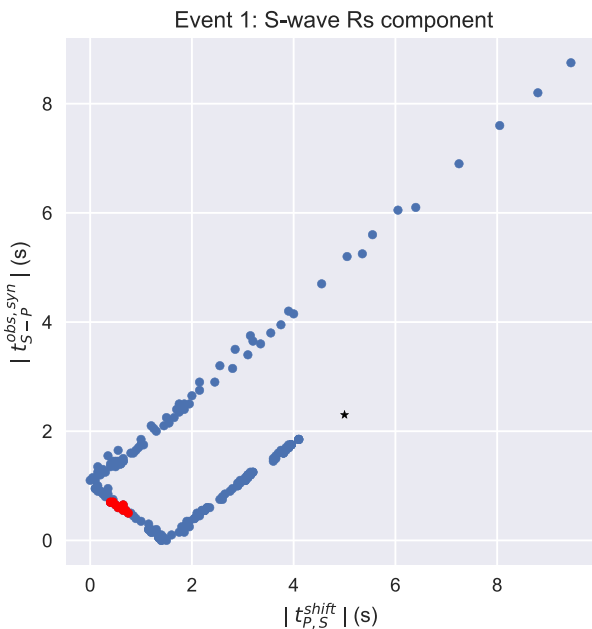


**Figure 8.** Plotting the absolute value of the travel time delay  $|t_{P,S}^{shift}|$  versus the absolute value of the differential travel time  $|t_{S-P}^{obs,syn}|$  for the radial component of the  $S$  wave arrival from the Bali Sea earthquake. Best-fit models by minimized RMS are displayed in red, whereas results for *ak135* are presented by a black star.

The data suggest that the most likely temperature conditions in the upper mantle beneath Réunion are  $T = 1400 - 1450^\circ\text{C}$ , with permeability coefficients in the range of  $k_0 = 10^{-5} - 10^{-6}\text{ m}^2$ . Equally minimizing  $t_{P,S}^{shift}$  and  $t_{S-P}^{obs,syn}$  through RMS has corrected for not being able to solve for the relative arrivals of the  $P$  and  $S$  waves and the position in time of the entire wave packet simultaneously. This gives more distinction in the temperature space, while losing some contrast along the permeability coefficients, because the effect of temperature on  $P$  and  $S$  wave velocities is close to linear and therefore has little effect on interphase differential travel times. This makes it a better measure of the position in time of the wave packet as a whole. If, on the other hand, we put 100% weight on  $t_{S-P}^{obs,syn}$ , then, we lose some constraint on fitting the entire wave packet in time but tighten the constraints on the relative traveltimes difference between phase arrivals. This in turn gives better distinction along the  $k_0$  range at the expense of  $T$ , because predominantly, the permeability coefficient controls interphase differential travel times. Both cases emphasize the favored scenarios of  $T = 1400 - 1450^\circ\text{C}$  and  $k_0 = 10^{-5} - 10^{-6}\text{ m}^2$ . Regardless of the weighting used for  $t_{P,S}^{shift}$  and  $t_{S-P}^{obs,syn}$  during the minimization process of the best-fit scenarios, the outcome remains robust despite slight redistribution of high temperatures and permeabilities.

Our predicted values for temperatures of  $T = 1400 - 1450^\circ\text{C}$  approach potential mantle temperatures for the lower end of MgO values suggested for primary magmas from Réunion (16% weight) at 1440–1480 °C, according to calculations from the MELTS numerical algorithm (Asimow et al., 2001; Ghiorso & Sack, 1995) and formulations of upper mantle potential temperatures (Herzberg et al., 2007). Temperature estimates from this study appear slightly too low to explain the full range of MgO values of up to 20% weight deduced from the Réunion transitional series, which indicate source temperatures up to 1650 °C (Sobolev & Nikogosian, 1994). However, this could be the result of the idealized melt microstructures adopted in our models. When performing parameter conversion, we assume a uniform network of organized cuspatate melt pockets that induce maximum seismic velocity reduction per percent melt, respectively, 3.6% and 7.9% for  $P$  and  $S$  waves in relaxed conditions (Hammond & Humphreys, 2000). Other melt pocket geometries, such as ellipsoidal or tubular shaped pore spaces, sustain lower velocity reductions per percent melt, namely, 2.1% and 4.3% for the former and 1.2% and 2.7% for the latter for the  $P$  and  $S$  waves. If we consider a nonuniformly distributed combination of pore geometries instead, we can expect overall a slightly lower effect of melt porosity on seismic velocity reduction. As a consequence, the best-fit scenarios will overcompensate

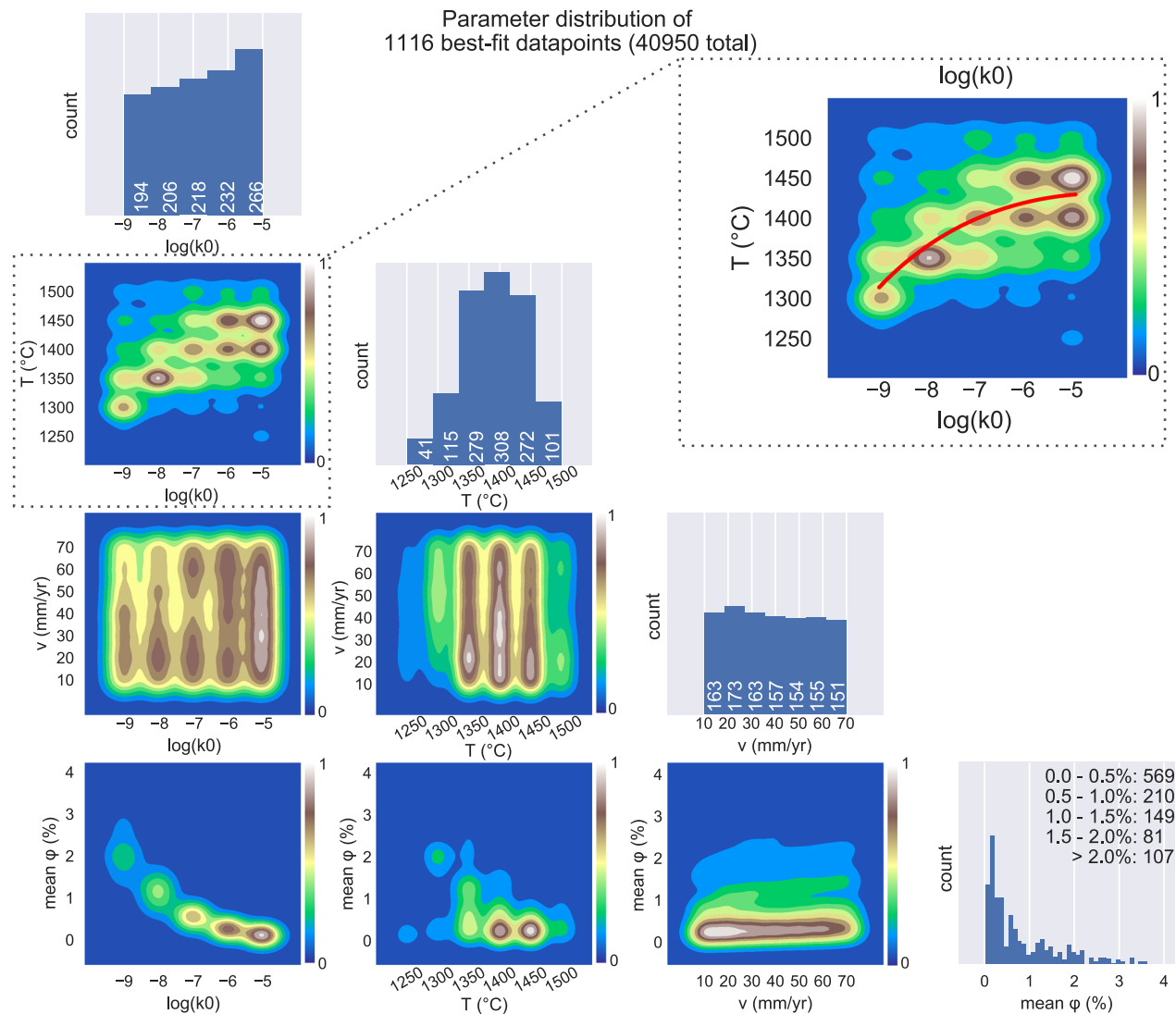


**Figure 9.** Pair grid plot displaying the distribution of permeability coefficient  $k_0$ , basal temperature  $T$ , upwelling velocity  $\bar{v}$ , and mean melt porosity  $\phi$  among the 1,116 best-fit travel time options out of 40,950 data points (2.7% of the data set with highest fit). Histograms on the diagonal count the representation of values for the variables  $k_0$ ,  $T$ ,  $\bar{v}$ , and  $\phi$  among 1,116 data points that have minimized  $t_{P,S}^{\text{shift}}$  and  $t_{S-P}^{\text{obs,syn}}$  with the observed traces. The off-diagonals show contour plots setting each of the input variables against each other, highlighting certain values within variable pairings that give a minimized solution to matching seismic travel times. The color scale shows relative density between minimum count and maximum count of the values for the variables in question, indicating which combination of values for any two variables is most likely to give a best-fit solution. Plotting temperature versus permeability coefficient shows the relationship between  $T$  and  $k_0$  in red for which relative travel times are minimized.

by either reducing the permeability coefficient or increasing temperature to attain a minimized travel time delay. This will cause greater polarization across the potential scenarios between the low porosity (high  $T$  and  $k_0$ ) and high porosity (low  $T$  and  $k_0$ ) cases, for which we have better constraints for high temperature.

For the predicted temperature values, the onset of melting is at 74.7- to 86.0-km depth for, respectively,  $T = 1400 - 1450^\circ\text{C}$ . This corresponds to a 60- to 90-km source depth for ultramafic melt that is proposed as origin of the ~2-km-thick underplated body observed at the base of the crust (Richards et al., 2013) and possibly aligns with depth of the LAB (Fontaine et al., 2015).

Values for the permeability coefficient predicted from the results for the upper mantle beneath Réunion are  $k_0 = 10^{-6} - 10^{-5}\text{ m}^2$ , which translate to upper mantle permeabilities of  $10^{-14} - 10^{-12}\text{ m}^2$  calculated for a porosity range of 0.13–0.28%. Coefficients of  $10^{-6}\text{ m}^2$  on average result in marginally better matches in time with the seismic observations and are more in line with experimental results of permeability in high-temperature high-pressure environments, at coefficients of  $2 \times 10^{-16}$  to  $5 \times 10^{-13}\text{ m}^2$  for porosity between

0.02 – 0.2 (Connolly et al., 2009). The mean melt transportation velocity values range in between 8.37 and 18.35 m·year<sup>-1</sup> for coefficients of, respectively,  $k_0 = 10^{-6} - 10^{-5}$  m<sup>2</sup>, approaching the lower melt flow rates of 20 m·year<sup>-1</sup> suggested by uranium isotope migration rates (Elliott & Spiegelman, 2003; Stracke et al., 2006). The model melt flow velocity could be higher if opting for a lower exponent  $n$  in the permeability-porosity relationship, where values down to 2 are within the accepted range for grain geometries in the upper mantle (Goes et al., 2012; Zhu & Hirth, 2003). By doing so, the predicted permeabilities will decrease to  $10^{-13} - 10^{-11}$  m<sup>2</sup> for  $n = 2$ , diverging from the earlier constraints put on permeability and only conceivable for coefficients of  $10^{-6}$  m<sup>2</sup>.

Across all source events, the mean traveltime difference and differential travel time for the best-fit model scenarios with  $T = 1400 - 1450$  °C and  $k_0 = 10^{-5} - 10^{-6}$  m<sup>2</sup> are  $t_{P,S}^{\text{shift}} = 0.06 \pm 0.51$  s and  $t_{S-P}^{\text{obs,syn}} = -0.20 \pm 0.46$  s, since within the majority of source events,  $t_{P,S}^{\text{shift}}$  and  $t_{S-P}^{\text{obs,syn}}$  do not simultaneously converge to 0 s. Overall, the synthetic phase arrival is slightly too early (i.e.,  $t_{P,S}^{\text{shift}}$  is positive) with respect to the observed, and therefore, the interphase differential travel time is slightly wider (i.e.,  $t_{S-P}^{\text{obs,syn}}$  is negative). Adopting a less idealized melt microstructure network will improve convergence toward 0 s, as it will slightly reduce the *P*-to-*S* velocity reduction ratio induced by melt and therefore reduce relative phase arrivals of compressional versus transverse waves. This relies on the assumption that the *ak135* reference model adequately approximates the geodynamical properties of the earth on a global scale and that the slight travel time discrepancy is a result of our presumptions on the modeled effect of melt on seismic wave propagation. It is likely that along each raypath for the studied source events, there are velocity anomalies with respect to the *ak135* reference model that are captured in our results through the misalignment in the  $t_{P,S}^{\text{shift}} - t_{S-P}^{\text{obs,syn}}$  relationship (Figure 8). The nature of the ratio between  $|t_{P,S}^{\text{shift}}|$  at  $t_{S-P}^{\text{obs,syn}} = 0$  and  $|t_{S-P}^{\text{obs,syn}}|$  at  $t_{P,S}^{\text{shift}} = 0$  s for each source event could tell something about the cause and magnitude of the velocity anomalies along the raypath. Furthermore, differences between the radial, transverse, and vertical seismic wave components could give insights on anisotropy within the velocity anomalies. When  $t_{S-P}^{\text{obs,syn}}$  does not converge to 0 s, it suggests that relative velocities between *P* and *S* waves are altered through any other means than melt presence as defined in this study. Local-scale heterogeneities such as lattice-preferred orientation of melt flow, shape preferred orientation of the pore geometry, crystalline anisotropy, or the presence of volatiles in the upper mantle could be relevant if there is notable heterogeneity along the raypaths between different seismic phases at seismic resolutions. When  $t_{P,S}^{\text{shift}}$  does not converge to 0 s, it indicates that the wave packet as a whole is either early or late with respect to the observations and could hint at large-scale heterogeneities along the raypaths such as large low-shear-velocity provinces, ultralow velocity zone, or mantle plumes. The general early phase arrival from the best-fit conditions could indicate a higher expected velocity anomaly from the Réunion mantle plume than modeled, but to identify the source, it would require extensive comparisons with tomographic cross sections along the raypaths for each source event.

## 6. Conclusion

In this study, we proposed a series of forward modeling in geodynamics and seismology in order to understand the direct link between the geodynamical parameters and seismic observation. We developed a partial melting model for the upper mantle in order to model melt porosity for 210 different combinations of permeability coefficients, temperature, and upwelling velocity. For each model scenario, synthetic seismograms were generated for 21 source events using the DSM with the *ak135* reference model as base model for global wave propagation. Analysis of travel time delay and interphase differential travel time of *P*, *Pdiff*, *S*, and *SKS* phase arrivals between synthetic waveforms and observed traces recorded at the RER GEOSCOPE receiver at Réunion allows us to statistically constrain several local geodynamic conditions in the upper mantle. Our results indicate that we are unable to constrain upwelling velocity but are able to constrain the most probable combination of temperature and permeability coefficient at  $T = 1400 - 1450$  °C and  $k_0 = 10^{-5} - 10^{-6}$  m<sup>2</sup>, which appear consistent with studies of potential mantle temperature based on MgO content. The proposed high permeabilities promote high rates of melt extraction at 8.37–18.35 m·year<sup>-1</sup>, which is in accordance with results from uranium isotope migration studies. Furthermore, from these predicted conditions follows that the onset of melting in the upper mantle beneath Réunion lies in between 74.7- and 86.0-km depth and most importantly that melt porosity does not exceed 0.28%.

Low velocity zones in the shallow upper mantle can be explained by a combination of relatively high mantle temperatures and low percentages of melt retention, which go hand in hand with rapid melt extraction as

a result of high permeability conditions in the melting zone. The results are able to satisfy prevalent geodynamical and geochemical predictions of low melt retention and high melt flow rate, while simultaneously adequately accounting for seismic data. We found that differences between travel time delay and interphase differential travel time of the synthetic traces versus the observed waveforms can indicate velocity anomalies along the raypath with respect to the base model and could potentially tell something about their nature.

## Appendix A: Inverse Versus Forward Problems in Geoscience

A conceptual representation of the classical method for exploration of the Earth's interior inherent to inversion procedures could be written as follows:

$$\mathbf{m}_{\text{inv}} = \mathcal{D}^\dagger \circ \mathcal{C}_S^D \circ (\mathcal{F}_{\text{comp}} \circ \mathcal{S})^\dagger \circ \mathcal{F}_{\text{obs}}(\mathbf{d}), \quad (\text{A1})$$

where  $\mathbf{m}_{\text{inv}}$  is a vector of estimated geodynamical model parameters that we look for,  $\mathbf{d}$  a vector of seismic observed waveforms, with  $\mathcal{D}$  the geodynamical modeling operator,  $\mathcal{C}_S^D$  parameter conversion operators from petrology to seismology,  $\mathcal{S}$  the seismic wave propagation operators, and  $\mathcal{F}_{\text{comp}}$  and  $\mathcal{F}_{\text{obs}}$  the seismic data processing operators applied to (or embedded in) computed data and observed data, respectively. All the operators above are essentially nonlinear in nature (occasionally linear, especially the seismic modeling operator  $\mathcal{F}_{\text{comp}} \circ \mathcal{S}$ ).  $^\dagger$  denotes “general inverse” of those operators. The reason why we precise the use of  $\mathcal{F}$  inside equation (A1) is our incapacity of modeling a whole series of seismic waveform data. When we measure only travel times  $\mathcal{F}_{\text{obs}}(\mathbf{d})$ , for instance, we use a linear Eikonal operator as  $\mathcal{F}_{\text{comp}} \circ \mathcal{S}$ . Indeed, due to the high-frequency approximation of wave equations in Eikonal equation,  $\mathcal{F}_{\text{comp}}$  can be different from  $\mathcal{F}_{\text{obs}}$ . Even wave-equation-based expensive operators  $\mathcal{F}_{\text{comp}} \circ \mathcal{S}$  (Geller & Takeuchi, 1998; Hasegawa et al., 2018; Komatitsch & Vilotte, 1998) are not an exception, the frequency contents and included physics will never meet the real Earth. Therefore, we have to (pre-)process the raw data  $\mathbf{d}$ . This discussion should be valid to some extent for other operators such as  $\mathcal{C}$  and  $\mathcal{D}$ , but for the simplicity, we do not discuss it in this paper. Equation (A1) reads as follows:

- (i) We collect the seismic raw waveforms  $\mathbf{d}$  from the existing stations.
- (ii) We filter the waveforms and/or picking travel times by cross correlations or handpicking of some phases of interest or surface-wave phase velocity picking, receiver function calculation, envelope calculation, or simply windowing of waveforms: We denote all the data processing symbolically as  $\mathcal{F}_{\text{obs}}(\mathbf{d})$  to distinguish the raw waveform data and the secondary seismic attributes to take into account.
- (iii) Seismic inversion is then applied to the seismic attributes in order to infer the inner structure of the Earth in terms of density, (an)isotropic seismic velocity, and seismic attenuation. This relies on the general inverse of forward modeling operators  $\mathcal{F}_{\text{obs}} \circ \mathcal{S}$  regardless of which propagation effects (e.g., full waveform or Eikonal's equation for ray tracing, 1D or 3D) are considered. In seismology, in general, we use some variations of quasi-Newton methods to linearize the inverse problem (French & Romanowicz, 2015; Fuji et al., 2010; Konishi et al., 2014; Marjanović et al., 2017; Xiao et al., 2020).
- (iv) Based on an understanding of petrology, we can interpret the ensemble of seismic parameters as geodynamically meaningful parameters such as temperature and chemical anomaly inside the mantle. Look-up tables of  $\mathcal{C}_S^D$  or  $\mathcal{C}_D^S$  are produced based on either in situ experiments or numerical simulation in petrology such as first-principles ab initio calculations (Deschamps et al., 2019; Konishi et al., 2020).
- (v) The geodynamicists can finally then seek the most probable scenario(s) of the Earth's inner evolution, mostly by trial-and-error forward modeling schemes and few by time-reversal or adjoint methods in geodynamics. Here, however, we denote this last step deliberately also as an inverse operator  $\mathcal{D}^\dagger$  since the aim is clearly to evaluate the misfit of the geodynamical models to seismic tomographic “observation”:

$$|\mathcal{D}(\mathbf{m}_{\text{inv}}) - \mathcal{C}_S^D \circ \mathcal{S}^\dagger \circ \mathcal{F}_{\text{obs}}(\mathbf{d})|^\alpha, \quad (\text{A2})$$

with  $\alpha$  a positive constant. We evaluate this misfit often in amplitude spectra or correlation domain (Steinberger & Torsvik, 2012). Atkins et al. (2016) and Shahnas et al. (2018) proposed a probabilistic inverse problem, by means of machine learning, to choose plausible scenarios  $\mathbf{m}_{\text{inv}}$  once we obtain tomographic “observation”  $\mathcal{C}_S^D \circ \mathcal{S}^\dagger \circ \mathcal{F}_{\text{obs}}(\mathbf{d})$ .

The workflow (equation A1) has been invaluable in geosciences since we have little data other than present-day seismological observation at seismic stations  $\mathbf{d}$  to infer the evolution of the Earth's mantle  $\mathbf{m}$ . Statistical confidence of the seismic model  $S^\dagger \circ \mathcal{F}_{\text{obs}}(\mathbf{d})$  has increased not only due to the increasing number of seismic stations, including ocean bottom seismic arrays, but also due to the theoretical and numerical improvement of  $\mathcal{F}_{\text{comp}} \circ S$  or a better estimation of  $(\mathcal{F}_{\text{comp}} \circ S)^\dagger$ .

The real data  $\mathbf{d}$  should be a function of the geodynamic parameters  $\mathbf{m}_{\text{true}}$ :

$$\mathbf{d} = S \circ C_D^S \circ D(\mathbf{m}_{\text{true}}). \quad (\text{A3})$$

The “estimated” geodynamical parameters  $\mathbf{m}_{\text{inv}}$  are therefore “low resolution filtered” as follows:

$$\mathbf{m}_{\text{inv}} = D^\dagger \circ C_S^D \circ S^\dagger \circ \mathcal{F}_{\text{comp}}^\dagger \circ \mathcal{F}_{\text{obs}} \circ S \circ C_D^S \circ D(\mathbf{m}_{\text{true}}). \quad (\text{A4})$$

When we consider only the seismic structure of the Earth's interior, the resolution operator,

$$\mathcal{R} = S^\dagger \circ \mathcal{F}_{\text{comp}}^\dagger \circ \mathcal{F}_{\text{obs}} \circ S, \quad (\text{A5})$$

is the same as the “seismic tomographic filter operator” proposed by Koelemeijer et al. (2018), Ritsema et al. (2007), and Schuberth et al. (2012). Evaluation of the “seismically filtered model”:

$$\mathbf{p} = \mathcal{R} \circ C_D^S \circ D(\mathbf{m}), \quad (\text{A6})$$

is interesting since it represents the sensitivity of our seismic tomographic model with respect to geodynamical model parameters.

Nevertheless, due to the nonlinearity of each forward operator and the approximations of its linearized inverse operator, it is difficult to quantitatively discuss the probability of proposed Earth's evolution scenarios. The only way to self-consistently answer this question is to directly model the full problem from first principles and compare the predicted data with the real data (equation A3), that is, predict a self-consistent thermochemical structure, then predict the seismic properties, and subsequently make a full comparison with the observation: the seismic signal received at the Earth's surface. We must perform every procedure in a forward manner. This approach could be more powerful and objective than a series of inversions (equation A1), in particular when we have concrete geodynamical parameters  $\mathbf{m}$  to look for.

Here in this paper, we propose to find the direct link between  $\mathbf{m}$  and  $\mathbf{d}$  by a series of forward modeling:

$$\mathbf{u} = S \circ C_D^S \circ D(\mathbf{m}), \quad (\text{A7})$$

with  $\mathbf{u}$  the “seismically filtered waveform data” instead of “seismically filtered model.” Sensitivity analysis of  $\mathbf{u}$  as a function of  $\mathbf{m}$  is more straightforward than the evaluation of  $\mathbf{p}$  in equation (A6). We then apply the  $\mathbf{u}$  with a new processing operator  $\mathcal{F}$  applied to synthetic and observed waveforms in order to compute the misfit function:

$$|\mathcal{F}(\mathbf{u}) - \mathcal{F}(\mathbf{d})|^\alpha = |\mathcal{F} \circ S \circ C_D^S \circ D(\mathbf{m}) - \mathcal{F}(\mathbf{d})|^\alpha. \quad (\text{A8})$$

The workflow presented in (A8) is represented in Figure 1. As the direct comparison between  $\mathbf{d}$  and  $\mathbf{u}$  is hard to realize, as is also the case in equation (A2), the choice of  $\mathcal{F}$  (the simplification of the problem) is the key. In Section 2, we will explain how to connectly realize the workflow (equation A8).

## References

- Armitage, J. J., Ferguson, D. J., Goes, S., Hammond, J., Calais, E., Rychert, C. A., & Harmon, N. (2015). Upper mantle temperature and the onset of extension and break-up in Afar, Africa. *Earth and Planetary Science Letters*, 418(Nature 465 2010), 78–90. <https://doi.org/10.1016/j.epsl.2015.02.039>
- Armitage, J. J., Petersen, K. D., & Marta, P. (2018). The role of crustal strength in controlling magmatism and melt chemistry during rifting and breakup. *Geochemistry, Geophysics, Geosystems*, 19, 534–550. <https://doi.org/10.1002/2017GC007326>
- Asimow, P., Hirschmann, M., & Stolper, E. (2001). Calculation of peridotite partial melting from thermodynamic models of minerals and melts. IV. Adiabatic decompression and the composition and mean properties of mid-ocean ridge basalts. *Journal of Petroleum*, 42(5), 963–998. <https://doi.org/10.1093/petrology/42.5.963>
- Atkins, S., Valentine, A. P., Tackley, P. J., & Trampert, J. (2016). Using pattern recognition to infer parameters governing mantle convection. *Physics of the Earth and Planetary Interiors*, 257, 171–186. <https://doi.org/10.1016/j.pepi.2016.05.016>

## Acknowledgments

This work was funded by the ANR grant Interrift. Numerical computations were partly performed on the S-CAPAD platform, IPGP, France. We acknowledge Incorporated Research Institutions for Seismology (IRIS) data center for RER station data (<https://doi.org/10.7914/SN/IU>). We also would like to thank Lapo Boschi, Saskia Goes, two anonymous reviewers, and the editors for their constructive comments. This is IPGP contribution 4133.

- Bormann, P. (Ed.) (2012). *New manual of seismological observatory practice (NMSOP-2)*. IASPEI, GFZ German Research Centre for Geosciences. <https://doi.org/10.2312/GFZ.NMSOP-2>
- Buland, R., & Chapman, C. H. (1983). The computation of seismic travel times. *Bulletin of the Seismological Society of America*, 73(5), 1271–1302.
- Burley, J., & Katz, R. F. (2015). Variations in mid-ocean ridge CO<sub>2</sub> emissions driven by glacial cycles. *Earth and Planetary Science Letters*, 426(Nature 421 6925 2003), 246–258. <https://doi.org/10.1016/j.epsl.2015.06.031>
- Cammarano, F., Goes, S., Vacher, P., & Giardini, D. (2003). Inferring upper-mantle temperatures from seismic velocities. *Physics of the Earth and Planetary Interiors*, 138(3-4), 197–222. [https://doi.org/10.1016/S0031-9201\(03\)00156-0](https://doi.org/10.1016/S0031-9201(03)00156-0)
- Chantel, J., Manthilake, G., Andrault, D., Novella, D., Yu, T., & Wang, Y. (2016). Experimental evidence supports mantle partial melting in the asthenosphere. *Science Advance*, 2(5), e1600246. <https://doi.org/10.1126/sciadv.1600246>
- Charvis, P., Laesapura, A., & Gallart, J. (1999). Spatial distribution of hotspot material added to the lithosphere under La Réunion, from wide-angle seismic data. *Journal of Geophysical Research*, 104(B2), 2875–2893. <https://doi.org/10.1029/98JB02841>
- Cobden, L., Trampert, J., & Fichtner, A. (2018). Insights on upper mantle melting, rheology, and anelastic behavior from seismic shear wave tomography. *Geochemistry, Geophysics, Geosystems*, 19, 3892–3916. <https://doi.org/10.1029/2017GC007370>
- Connolly, J. A. D. (2005). Computation of phase equilibria by linear programming: A tool for geodynamic modeling and its application to subduction zone decarbonation. *Earth and Planetary Science Letters*, 236(1-2), 524–541.
- Connolly, J., Schmidt, M., Solferino, G., & Bagdassarov, N. (2009). Permeability of asthenospheric mantle and melt extraction rates at mid-ocean ridges. *Nature*, 462(7270), 209–212. <https://doi.org/10.1016/j.epsl.2009.04.033>
- Courtillot, V., Davaille, A., Besse, J., & Stock, J. (2003). Three distinct types of hotspots in the Earth's mantle. *Earth and Planetary Science Letters*, 205(3-4), 295–308. [https://doi.org/10.1016/S0016-801X\(02\)01048-8](https://doi.org/10.1016/S0016-801X(02)01048-8)
- Crotwell, H. P., Owens, T. J., & Ritsema, J. (1999). The TauP toolkit: Flexible seismic travel-time and ray-path utilities. *Seismological Research Letters*, 70(2), 154–160. <https://doi.org/10.1785/gssrl.70.2.154>
- Cummins, P., Takeuchi, N., & Geller, R. (1997). Computation of complete synthetic seismograms for laterally heterogeneous models using the direct solution method. *Geophysical Journal International*, 130(1), 1–16. <https://doi.org/10.1111/j.1365-246X.1997.tb00983.x>
- Deschamps, F., Konishi, K., Fuji, N., & Cobden, L. (2019). Radial thermo-chemical structure beneath western and northern Pacific from seismic waveform inversion. *Earth and Planetary Science Letters*, 520, 153–163. <https://doi.org/10.1016/j.epsl.2019.05.040>
- Douet, V., Vallée, M., Zigone, D., Bonaimé, S., Stutzmann, E., Maggi, A., et al. (2016). The geoscope broadband seismic observatory. In *Egu general assembly conference abstracts*, 18.
- Duncan, R. A., & Hargraves, R. B. (1990). <sup>40</sup>Ar/<sup>39</sup>Ar geochronology of basement rocks from the Mascarene Plateau, the Chagos Bank, and the Maldives Ridge. *Proceedings Ocean Drilling Program Science Results*, 115, 43–51.
- Eilon, Z. C., & Abers, G. A. (2017). High seismic attenuation at a mid-ocean ridge reveals the distribution of deep melt. *Science Advance*, 3(5), e1602829. <https://doi.org/10.1126/sciadv.1602829>
- Elliott, T., & Spiegelman, M. (2003). Melt migration in oceanic crustal production: A U-series perspective. In D. H. Heinrich, R. L. Rudnick, & K. K. Turekian (Eds.), *Treatise on geochemistry*. Pergamon: Elsevier, pp. 465–510.
- Fontaine, F. R., Barruol, G., Tkalčić, H., H., Wölbren, I., Rümpker, G., Bodin, T., & Haugard, M. (2015). Crustal and uppermost mantle structure variation beneath La Réunion hotspot track. *Geophysical Journal International*, 203(1), 107–126. <https://doi.org/10.1093/gji/gjv279>
- Forsyth, D. W. (1998). Imaging the deep seismic structure beneath a mid-ocean ridge: The MELT experiment. *Science*, 280(5367), 1215–1218. <https://doi.org/10.1126/science.280.5367.1215>
- French, S., & Romanowicz, B. (2015). Broad plumes rooted at the base of the Earth's mantle beneath major hotspots. *Nature*, 525, 95–99.
- Fuji, N., Chevrot, S., Zhao, L., Geller, R. J., & Kawai, K. (2012). Finite-frequency structural sensitivities of short-period compressional body waves. *Geophysical Journal International*, 190(1), 522–540. <https://doi.org/10.1111/j.1365-246X.2012.05495.x>
- Fuji, N., Kawai, K., & Geller, R. J. (2010). A methodology for inversion of broadband seismic waveforms for elastic and anelastic structure and its application to the mantle transition zone beneath the northwestern Pacific. *Physics of the Earth and Planetary Interiors*, 180, 118–137.
- Gallart, J., Driadi, L., Charvis, P., & Sapin, M. (1999). Perturbation to the lithosphere along the hotspot track of La Réunion from an offshore-onshore seismic transect. *Journal of Geophysical Research*, 104(B2), 2895–2908.
- Geller, R., & Ohminato, T. (1994). Computation of synthetic seismograms and their partial derivatives for heterogeneous media with arbitrary natural boundary conditions using the direct solution method. *Geophysical Journal International*, 116, 421–446.
- Geller, R., & Takeuchi, N. (1995). A new method for computing highly accurate DSM synthetic seismograms. *Geophysical Journal International*, 123, 449–470. <https://doi.org/10.1111/j.1365-246X.1995.tb06865.x>
- Geller, R., & Takeuchi, N. (1998). Optimally accurate second-order time-domain finite difference scheme for the elastic equation of motion: One-dimensional cases. *Geophysical Journal International*, 135, 48–62.
- Ghiorso, M. S., & Sack, R. O. (1995). Chemical mass transfer in magmatic processes IV. A revised and internally consistent thermodynamic model for the interpolation and extrapolation of liquid-solid equilibria in magmatic systems at elevated temperatures and pressures. *Contributions to Mineralogy and Petrology*, 119(2-3), 197–212. <https://doi.org/10.1007/BF00307281>
- Goess, S., Armitage, J., Harmon, N., Smith, H., & Huismans, R. (2012). Low seismic velocities below mid-ocean ridges: Attenuation versus melt retention. *Journal of Geophysical Research*, 117, B12403. <https://doi.org/10.1029/2012JB009637>
- Hammond, W. C., & Humphreys, E. D. (2000). Upper mantle seismic wave velocity: Effects of realistic partial melt geometries. *Journal of Geophysical Research*, 105(B5), 10,975–10,986. <https://doi.org/10.1029/2000JB900041>
- Harmon, N., Forsyth, D. W., & Weeraratne, D. S. (2009). Thickening of young Pacific lithosphere from high-resolution Rayleigh wave tomography: A test of the conductive cooling model. *Earth and Planetary Science Letters*, 278(1-2), 96–106. <https://doi.org/10.1016/j.epsl.2008.11.025>
- Hasegawa, K., Fuji, N., & Konishi, K. (2018). Improvement of accuracy of the spectral element method for elastic wave computation using modified numerical integration operators. *Computer Methods in Applied Mechanics and Engineering*, 342, 200–223.
- Havlin, C., & Parmentier, E. M. (2014). Implications for melt transport and source heterogeneity in upwelling mantle from the magnitude of  $S_p$  converted phases generated at the onset of melting. *Geophysical Research Letters*, 41, 5444–5450. <https://doi.org/10.1002/2014GL060890>
- Herzberg, C., Asimow, P. D., Arndt, N., Niu, Y., Lesher, C. M., Fitton, J. G., et al. (2007). Temperatures in ambient mantle and plumes: Constraints from basalts, picrites, and komatiites. *Geochemistry, Geophysics, Geosystems*, 8, Q02006. <https://doi.org/10.1029/2006GC001390>
- Herzberg, C., Asimow, P. D., Ionov, D. A., Vidito, C., Jackson, M. G., & Geist, D. (2013). Nickel and helium evidence for melt above the core-mantle boundary. *Nature*, 493(7432), 393–397. <https://doi.org/10.1029/2006GC001390>

- Hewitt, I. J. (2010). Modelling melting rates in upwelling mantle. *Earth and Planetary Science Letters*, 300(3-4), 264–274. <https://doi.org/10.1016/j.epsl.2010.10.010>
- Hirose, K., & Kushiro, I. (1993). Partial melting of dry peridotites at high pressures: Determination of compositions of melts segregated from peridotite using aggregates of diamond. *Earth and Planetary Science Letters*, 114(4), 477–489. [https://doi.org/10.1016/0012-821X\(93\)90077-M](https://doi.org/10.1016/0012-821X(93)90077-M)
- Hirschmann, M. M., Ghiors, M. S., & Stolper, M. (1999). Calculation of peridotite partial melting from thermodynamic models of minerals and melts. II. Isobaric variations in melts near the solidus and owing to variable source composition. *Journal of Petroleum*, 40(2), 297–313. <https://doi.org/10.1093/petroj/40.2.297>
- Hirschmann, M., Tenner, T., Aubaud, C., & Withers, A. C. (2009). Dehydration melting of nominally anhydrous mantle: The primacy of partitioning. *Physics of the Earth and Planetary Interiors*, 176(1-2), 54–68. <https://doi.org/10.1016/j.pepi.2009.04.001>
- Karato, S. (1993). Importance of anelasticity in the interpretation of seismic tomography. *Geophysical Research Letters*, 20, 1623–1626. <https://doi.org/10.1029/93GL01767>
- Karato, S.-i. (2014). Does partial melting explain geophysical anomalies? *Physics of the Earth and Planetary Interiors*, 228, 300–306. <https://doi.org/10.1016/j.pepi.2013.08.006>
- Katz, R. F., Spiegelman, M., & Langmuir, C. H. (2003). A new parameterization of hydrous mantle melting. *Geochemistry, Geophysics, Geosystems*, 4(9), 1073. <https://doi.org/10.1029/2002GC000433>
- Kawai, K., Takeuchi, N., & Geller, R. J. (2006). Complete synthetic seismograms up to 2 Hz for transversely isotropic spherically symmetric media. *Geophysical Journal International*, 164(2), 411–424. <https://doi.org/10.1111/j.1365-246X.2005.02829.x>
- Kennett, B., Engdahl, E., & Buland, R. (1995). Constraints on seismic velocities in the Earth from traveltimes. *Geophysical Journal International*, 122(1), 108–124. <https://doi.org/10.1111/j.1365-246X.1995.tb03540.x>
- Koelemeijer, P., Schuberth, B. S. A., Davies, D. R., Deuss, A., & Ritsema, J. (2018). Constraints on the presence of post-perovskite in Earth's lowermost mantle from tomographic-geodynamic model comparisons. *Earth and Planetary Science Letters*, 494, 226–238.
- Komatitsch, D., & Vilotte, J. P. (1998). The spectral element method: An efficient tool to simulate the seismic response of 2D and 3D geological structures. *Bulletin of the Seismological Society of America*, 88, 368–392.
- Konishi, K., Fuji, N., & Deschamps, F. (2020). Three-dimensional elastic and anelastic structure of the lowermost mantle beneath the western Pacific from finite-frequency tomography. *Journal of Geophysical Research: Solid Earth*, 125, e2019JB018089. <https://doi.org/10.1029/2019JB018089>
- Konishi, K., Kawai, K., Geller, R. J., & Fuji, N. (2014). Waveform inversion for localized three-dimensional seismic velocity structure in the lowermost mantle beneath the western Pacific. *Geophysical Journal International*, 199, 1245–1267.
- Marjanović, M., Fuji, N., Singh, S. C., Belahi, T., & Escartin, J. (2017). Seismic signatures of hydrothermal pathways along the east Pacific rise between 9° 16' E and 9° 56' N. *Journal of Geophysical Research: Solid Earth*, 122, 10,241–10,262. <https://doi.org/10.1002/2017JB015004>
- Mazzullo, A., Stutzmann, E., Montagner, J. P., Kiselev, S., Maurya, S., Barruol, G., & Sigloch, K. (2017). Anisotropic tomography around La Réunion island from Rayleigh waves. *Journal of Geophysical Research: Solid Earth*, 122, 9132–9148. <https://doi.org/10.1002/2017JB014354>
- McKenzie, D. (1984). The generation and compaction of partially molten rock. *Journal of Petroleum*, 25(3), 713–765. <https://doi.org/10.1093/petrology/25.3.713>
- Mehouachi, F., & Singh, S. C. (2018). Water-rich sublithospheric melt channel in the equatorial Atlantic ocean. *Nature Geoscience*, 11(1), 65–69. <https://doi.org/10.1038/s41561-017-0034-z>
- Miller, K. J., Zhu, Wen-lu, Montési, L., & Gaetani, G. A. (2014). Experimental quantification of permeability of partially molten mantle rock. *Earth and Planetary Science Letters*, 388, 273–282. <https://doi.org/10.1016/j.epsl.2013.12.003>
- Monteiller, V., Chevrot, S., Komatitsch, D., & Wang, Y. (2015). Three-dimensional full waveform inversion of short-period teleseismic wavefields based upon the SEM-DSM hybrid method. *Geophysical Journal International*, 202(2), 811–827.
- Morgan, J. (2001). Thermodynamics of pressure release melting of a veined plum pudding mantle. *Geochemistry Geophysics Geosystems*, 2(4), 1001. <https://doi.org/10.1029/2000GC000049>
- Ribe, N. M. (1985). The deformation and compaction of partial molten zones. *Geophysical Journal International*, 83, 487–501. <https://doi.org/10.1111/j.1365-246X.1985.tb06499.x>
- Richards, M. A., Duncan, R. A., & Science, V. E. (1989). Flood basalts and hot-spot tracks: Plume heads and tails. *Science*, 246, 103–107. <https://doi.org/10.1126/science.246.4926.103>
- Richards, M., Eduardo, C. R., Carolina, L. B., Ghiors, M., & Stixrude, L. (2013). Petrological interpretation of deep crustal intrusive bodies beneath oceanic hotspot provinces. *Geochemistry Geophysics Geosystems*, 14, 604–619. <https://doi.org/10.1029/2012GC004448>
- Ritsema, J., McNamara, A. K., & Bull, A. L. (2007). Tomographic filtering of geodynamic models: Implications for model interpretation and large-scale mantle structure. *Journal of Geophysical Research*, 112, B01303. <https://doi.org/10.1029/2006JB004566>
- Rychert, C. A., Hammond, J. O. S., Harmon, N., Kendall, M. J., Keir, D., Ebinger, C., et al. (2012). Volcanism in the Afar rift sustained by decompression melting with minimal plume influence. *Nature Geoscience*, 5(6), 406–409. <https://doi.org/10.1038/ngeo1455>
- Rychert, C. A., Harmon, N., & Ebinger, C. (2014). Receiver function imaging of lithospheric structure and the onset of melting beneath the Galápagos archipelago. *Earth and Planetary Science Letters*, 388, 156–165. <https://doi.org/10.1016/j.epsl.2013.11.027>
- Rychert, C. A., Laske, G., Harmon, N., & Shearer, P. M. (2013). Seismic imaging of melt in a displaced Hawaiian plume. *Nature Geoscience*, 6(8), 657–660. <https://doi.org/10.1038/ngeo1878>
- Schuberth, B. S. A., Zaroli, C., & Nolet, G. (2012). Synthetic seismograms for a synthetic earth: Long-period P and wave traveltimes variations can be explained by temperature alone. *Geophysical Journal International*, 188(3), 1393–1412. <https://doi.org/10.1111/j.1365-246X.2011.05333.x>
- Scott, D. R. (1992). Small-scale convection and mantle melting beneath mid-ocean ridges. In J. P. Morgan, D. K. Blackman, & J. M. Sinton (Eds.), *Mantle flow and melt generation at mid-ocean ridges* (pp. 327–352). Washington DC: American Geophysical Union.
- Shahnas, M. H., Yuen, D. A., & Pysklywec, R. N. (2018). Inverse problems in geodynamics using machine learning algorithms. *Journal of Geophysical Research: Solid Earth*, 123, 296–310. <https://doi.org/10.1002/2017JB014846>
- Sobolev, A. V., & Nikogosian, I. K. (1994). Petrology of long-lived mantle plume magmatism: Hawaii, Pacific and Reunion island, Indian ocean. *Petrology*, 2, 111–144.
- Steinberger, B., & Torsvik, T. H. (2012). A geodynamic model of plumes from the margins of large low shear velocity provinces. *Geochemistry, Geophysics, Geosystems*, 13, Q01W09. <https://doi.org/10.1029/2011GC003808>
- Stixrude, L., & Lithgow-Bertelloni, C. (2005). Thermodynamics of mantle minerals I. Physical properties. *Geophysical Journal International*, 162(2), 610–632. <https://doi.org/10.1111/j.1365-246X.2005.02642.x>
- Stracke, A., Bourdon, B., & Dan, M. (2006). Melt extraction in the Earth's mantle: Constraints from U-Th-Pa-Ra studies in oceanic basalts. *Earth and Planetary Science Letters*, 244(1-2), 97–112. <https://doi.org/10.1016/j.epsl.2006.01.057>

- Vallée, M., & Douet, V. (2016). A new database of source time functions (STFs) extracted from the SCARDEC method. *Physics of the Earth and Planetary Interiors*, 257, 149–157. <https://doi.org/10.1016/j.pepi.2016.05.012>
- Weatherley, S. M., & Katz, R. F. (2016). Melt transport rates in heterogeneous mantle beneath mid-ocean ridges. *Geochimica et Cosmochimica Acta*, 172, 39–54. <https://doi.org/10.1016/j.gca.2015.09.029>
- Xiao, Z., Fuji, N., Iidaka, T., Gao, Y., Sun, X., & Liu, Q. (2020). Seismic structure beneath the Tibetan Plateau from iterative finite-frequency tomography based on ChinArray: New insights into the Indo-Asian collision. *Journal of Geophysical Research: Solid Earth*, 125, e2019JB018344. <https://doi.org/10.1029/2019JB018344>
- Xu, W., Lithgow-Bertelloni, C., Sixtrude, L., & Ritsema, J. (2008). The effect of bulk composition and temperature on mantle seismic structure. *Earth and Planetary Science Letters*, 275, 70–79. <https://doi.org/10.1016/j.epsl.2008.08.012>
- Zhu, W., & Hirth, G. (2003). A network model for permeability in partially molten rocks. *Earth and Planetary Science Letters*, 212(3-4), 407–416. [https://doi.org/10.1016/S0012-821X\(03\)00264-4](https://doi.org/10.1016/S0012-821X(03)00264-4)